








Article

Increased Cytotoxicity of Bimetallic Ultrasmall Silver–Platinum Nanoparticles (2 nm) on Cells and Bacteria in Comparison to Silver Nanoparticles of the Same Size

Natalie Wolff ¹, Nataniel Białas ¹ , Kateryna Loza ¹, Marc Heggen ², Torsten Schaller ³, Felix Niemeyer ³, Claudia Weidenthaler ⁴ , Christine Beuck ⁵ , Peter Bayer ⁵ , Oleg Prymak ¹ , Cristiano L. P. Oliveira ⁶  and Matthias Epple ^{1,*} 

- ¹ Inorganic Chemistry and Centre for Nanointegration Duisburg-Essen (CENIDE), University of Duisburg-Essen, Universitaetsstr. 5-7, 45117 Essen, Germany; natalie.wolff@uni-due.de (N.W.); nataniel.bialas@uni-due.de (N.B.); kateryna.loza@uni-due.de (K.L.); oleg.prymak@uni-due.de (O.P.)
- ² Ernst Ruska Centre for Microscopy and Spectroscopy with Electrons, Forschungszentrum Jülich, 52428 Jülich, Germany; m.heggen@fz-juelich.de
- ³ Organic Chemistry, University of Duisburg-Essen, Universitaetsstr. 5-7, 45117 Essen, Germany; torsten.schaller@uni-due.de (T.S.); felix.niemeyer@uni-due.de (F.N.)
- ⁴ Max-Planck-Institut für Kohlenforschung, 45470 Mülheim an der Ruhr, Germany; weidenthaler@mpi-muelheim.mpg.de
- ⁵ Institute of Biology and Center for Medical Biotechnology (ZMB), University of Duisburg-Essen, Universitaetsstr. 5-7, 45117 Essen, Germany; christine.beuck@uni-due.de (C.B.); peter.bayer@uni-due.de (P.B.)
- ⁶ Institute of Physics, University of São Paulo, São Paulo 05508-090, Brazil; crislopo@if.usp.br
- * Correspondence: matthias.epple@uni-due.de



Citation: Wolff, N.; Białas, N.; Loza, K.; Heggen, M.; Schaller, T.; Niemeyer, F.; Weidenthaler, C.; Beuck, C.; Bayer, P.; Prymak, O.; et al. Increased Cytotoxicity of Bimetallic Ultrasmall Silver–Platinum Nanoparticles (2 nm) on Cells and Bacteria in Comparison to Silver Nanoparticles of the Same Size. *Materials* **2024**, *17*, 3702. <https://doi.org/10.3390/ma17153702>

Academic Editor: Aivaras Kareiva

Received: 8 July 2024

Revised: 19 July 2024

Accepted: 24 July 2024

Published: 26 July 2024



Copyright: © 2024 by the authors. Licensee MDPI, Basel, Switzerland. This article is an open access article distributed under the terms and conditions of the Creative Commons Attribution (CC BY) license (<https://creativecommons.org/licenses/by/4.0/>).

Abstract: Ultrasmall nanoparticles (diameter 2 nm) of silver, platinum, and bimetallic nanoparticles (molar ratio of Ag:Pt 0:100; 20:80; 50:50; 70:30; 100:0), stabilized by the thiolated ligand glutathione, were prepared and characterized by transmission electron microscopy, differential centrifugal sedimentation, X-ray photoelectron spectroscopy, small-angle X-ray scattering, X-ray powder diffraction, and NMR spectroscopy in aqueous dispersion. Gold nanoparticles of the same size were prepared as control. The particles were fluorescently labeled by conjugation of the dye AlexaFluor-647 via copper-catalyzed azide-alkyne cycloaddition after converting amine groups of glutathione into azide groups. All nanoparticles were well taken up by HeLa cells. The cytotoxicity was assessed with an MTT test on HeLa cells and minimal inhibitory concentration (MIC) tests on the bacteria *Escherichia coli* and *Staphylococcus xylosum*. Notably, bimetallic AgPt nanoparticles had a higher cytotoxicity against cells and bacteria than monometallic silver nanoparticles or a physical mixture of silver and platinum nanoparticles. However, the measured release of silver ions from monometallic and bimetallic silver nanoparticles in water was very low despite the ultrasmall size and the associated high specific surface area. This is probably due to the surface protection by a dense layer of thiolated ligand glutathione. Thus, the enhanced cytotoxicity of bimetallic AgPt nanoparticles is caused by the biological environment in cell culture media, together with a polarization of silver by platinum.

Keywords: nanoparticles; silver; gold; platinum; cytotoxicity; antibacterial effects

1. Introduction

Nanoparticles are the basis of nanomedicine, i.e., the targeted delivery of drugs by therapeutic or theranostic nanoparticles [1–4]. Imaging is also possible with the application of suitably functionalized nanoparticles [5–7]. Another important area is the fight against pathogenic bacteria, e.g., during implant-associated infections. Here, nanoparticles with bactericidal properties represent a promising alternative to antibiotics [8,9]. One approach is to use nanoparticles as carriers of drugs against bacteria, and an alternative is the controlled release of bactericidal ions like silver or copper to exert a specific bactericidal action.

Silver nanoparticles have gained some prominence in this field due to their well-known antibacterial effect [10–13]. However, it has been demonstrated that silver ions are toxic against eukaryotic cells (e.g., healthy tissue) as well [14]. An alternative approach is to prepare bimetallic nanoparticles where silver is mixed with a nobler metal like gold [15–20] or platinum [21–23]. Another option is to make the nanoparticles very small so that they are more mobile in the body and less prone to form a protein corona on their surface [24].

Here, we present the biological effects of ultrasmall bimetallic silver–platinum nanoparticles with variable metal ratio (diameter about 2 nm), coated with glutathione (GSH), and compare their bactericidal effect with the cytotoxic effect against eukaryotic cells. In addition, monometallic nanoparticles of silver, platinum, and gold (as control) of the same size were studied, as well as a physical mixture of silver and platinum nanoparticles.

2. Materials and Methods

2.1. Chemicals and Reagents

Ultrapure water prepared with a Purelab ultra instrument (ELGA, Celle, Germany) with a specific resistivity of 18.2 M Ω was used for all syntheses and analyses, unless otherwise noted. All glassware for the syntheses was cleaned with boiling *aqua regia* and rinsed twice with water before use.

As metal precursors, silver nitrate (AgNO₃, 99%, Carl Roth, Karlsruhe, Germany), hexachloridoplatinum(+IV) acid (H₂PtCl₆, 8 wt% in H₂O; Sigma-Aldrich, Steinheim, Germany), and tetrachloridoauric(+III) acid (HAuCl₄; prepared by dissolution of elemental gold in *aqua regia*) were used. Sodium borohydride (NaBH₄, 96%), L-glutathione (GSH, 98%), copper(II)sulfate pentahydrate (>99%), sodium L-ascorbate (>99%), and Spin-X[®] UF 30 kDa MWCO PES spin filters (Corning[®]) were obtained from Sigma-Aldrich. Sodium hydroxide (NaOH, 1 M), hydrochloric acid (HCl, 37%), and nitric acid (HNO₃, 67%) were obtained from Bernd Kraft (Duisburg, Germany). Methanol (99.8%) was obtained from FisherScientific (Geel, Belgium). Aminoguanidine hydrogen carbonate (98%) was obtained from Alfa Aesar (Kandel, Germany). Tris(3-hydroxypropyltriazolylmethyl)amine (TH-PTA, >95%) and AlexaFluor-647-alkyne (95%) were obtained from Jena Bioscience (Jena, Germany). Dodecane (99%) and 2-(4,5-dimethylthiazol-2-yl)-3,5-diphenyl-2H-tetrazol-3-ium bromide (MTT) were obtained from ThermoFisher Scientific (Schwerte, Germany). Dimethyl sulfoxide (DMSO, >99.5%) was obtained from Carl Roth. For differential centrifugal sedimentation (DCS), a PVC nanoparticle calibration dispersion (Lot#149, 1.385 g L^{−1}) was obtained from CPS Instruments Inc. (Oosterhout, The Netherlands). Deuterium oxide (D₂O, 99.9%) was obtained from Deutero GmbH (Kastellaun, Germany). 10 kDa spin filters were obtained from Merck (Darmstadt, Germany). Imidazole-1-sulfonyl azide hydrogen sulfate was prepared as reported earlier [25].

2.2. Electron Microscopy

High-resolution transmission electron microscopy (HRTEM) was carried out with an FEI Titan transmission electron microscope (ThermoFisher, Schwerte, Germany, which was aberration-corrected with a Cs-probe corrector (CEOS Company, Heidelberg, Germany) and operated at an accelerating voltage of 300 kV [26]. The nanoparticles were dispersed in water, followed by placing a drop of the suspension onto a carbon-coated copper grid and allowing it to dry under ambient conditions. The core diameter was determined manually by measuring the size of at least 100 particles from different HRTEM images.

2.3. X-ray Powder Diffraction (XRD)

X-ray powder diffraction (XRD) was performed with a Bruker D8 Advance diffractometer (Bruker Company, Billerica, MA, USA), with Cu K α radiation ($\lambda = 1.54 \text{ \AA}$) operating at 40 kV and 40 mA. A dispersion of nanoparticles was placed on a silicon single-crystal sample holder to minimize scattering and dried in air. The samples were measured in reflection mode from 20 to 90° 2 Θ with a step size of 0.02° and a counting time of 8 s per step. This resulted in a total measurement time of 500 min. Qualitative phase analysis was

performed with Diffrac.Suite EVA V1.2 from Bruker with the patterns of the metals Ag (#04-0783) and Pt (#04-0802) and their oxides Ag₂O (#41-1104) and PtO (#47-1171) from the ICDD database.

2.4. Small-Angle X-ray Scattering (SAXS)

Small-angle X-ray scattering was performed at the EMUSAXS center of the Institute of Physics, University of São Paulo. The laboratory-based equipment Xeuss 2.0 was used for the data acquisition. The source was a Genix3D Cu K α X-ray tube ($\lambda = 1.5418 \text{ \AA}$), equipped with a Focus3D mirror. The beam was collimated with two sets of scatterless slits, leading to a beam size of $0.7 \times 0.7 \text{ mm}^2$. The 2D scattering images were collected on a Dectris-Pilatus 300k detector placed at a 537 mm distance from the sample. The images were integrated with the program Fit2D [27]. 1D curves of the intensity as function of the reciprocal space momentum transfer modulus q were obtained. q is defined as $q = 4\pi \sin(\theta)/\lambda$, where θ is the scattering angle. The liquid samples (nanoparticles dispersed in water) were placed on reusable sample holders composed of borosilicate glass capillaries (Hilgenberg, Germany) of 1.5 mm diameter, glued on stainless steel cases. The holder was closed with rubber caps which allowed the measurements in vacuum. In this way, samples and blank were measured under exactly the same conditions, which is crucial for the proper data treatment. The data treatment was performed with the program SuperSAXS [28] using plain water as blank. The scattering from water was also used for absolute scale normalization.

The scattering data were analyzed by a polydisperse hard spheres model, as already used in previous work with nanoparticles [29]. In this model, the particles are described with a central radius R , a polydispersity σ , a hard spheres interaction radius R_{HS} , and a volume fraction η .

2.5. NMR Spectroscopy

Proton and carbon nuclear magnetic resonance (NMR) analyses were conducted with a Bruker AVIII HD spectrometer (Bruker Company, Billerica, MA, USA). The spectrometer was equipped with a nitrogen-cooled probe and operated at 600.13 MHz for ¹H and 150.90 MHz for ¹³C. For ¹H NMR acquisition, the excitation sculpting technique to attenuate the solvent's signal was used. Similarly, water signal pre-saturation was employed during COSY, HSQC, and HMBC experiments to achieve analogous suppression.

2.6. DOSY-NMR Spectroscopy

DOSY-NMR spectroscopy was performed and analyzed as previously described [30] on a Bruker Avance III 700 MHz spectrometer (Bruker Company, Billerica, MA, USA) equipped with a 5 mm TCI cryoprobe with a z-gradient at 25 °C. ¹H DOSY spectra were recorded with a diffusion time of $\Delta = 100 \text{ ms}$, a pulsed gradient duration of $\delta = 3.5 \text{ ms}$, and the gradient strength ranging from 5–95% of the maximum (66 G cm^{-1}) in 32 steps. Spectra were processed with Topspin 3.5 (Bruker). The linearized diffusion data were analyzed according to the Stejskal–Tanner equation [31,32]:

$$\ln\left(\frac{I}{I_0}\right) = -\gamma^2 \cdot \delta^2 \cdot \left(\Delta - \frac{\delta}{3}\right) \cdot D \cdot G^2 \quad (1)$$

with I the signal intensity, I_0 the signal intensity without gradient, γ the gyromagnetic ratio of ¹H, δ the diffusion gradient pulse length, Δ the diffusion delay, G the gradient strength, and D the translational diffusion coefficient.

The Stejskal–Tanner plots for three GSH signals (H1/H6 3.8 ppm, H4 2.6 ppm, 2.2 ppm) were first analyzed separately. Then, the data points of all three signals were averaged, with the error bars representing their standard deviation. While the intrinsic standard error of the Stejskal–Tanner fit is small (<2%), we estimate the error of the diffusion coefficient to about 20% due to the manual integration and potential overlaying of small signals from impurities.

The hydrodynamic diameter was calculated according to the Stokes–Einstein equation [33]:

$$d_H = \frac{k_B \cdot T}{3 \cdot \pi \cdot \eta \cdot D} \quad (2)$$

with d_H the hydrodynamic diameter, k_B the Boltzmann constant, T the temperature in K, η the dynamic viscosity at 25 °C, and D the translational diffusion coefficient.

2.7. X-ray Photoelectron Spectroscopy (XPS)

X-ray photoelectron spectroscopy (XPS) was performed with a SPECS spectrometer (SPECS Surface Nano Analysis GmbH, Berlin, Germany), which was equipped with a Phoibos 150 1D-DLD hemispherical energy analyzer. The monochromatized Al K α X-ray source ($E = 1486.6$ eV) was operated at 15 kV and 200 W. The pass energy was set to 20 eV for high-resolution scans, and the medium area mode was used as lens mode. The base pressure in the analysis chamber was set to $1 \cdot 10^{-10}$ mbar during the experiment. All spectra were referred to C 1s at 284.5 eV to account for charging effects. The spectra were evaluated with the CasaXPS software v2.3.26rev1.1s [34].

2.8. Elemental Analysis (AAS, ICP-MS)

Atomic absorption spectroscopy (AAS) with a Thermo Electron M-series spectrometer (ThermoFisher, Schwerte, Germany) graphite tube furnace, operated in accordance with DIN EN ISO/IEC 17025:2005), was used to determine the concentrations of Ag, Au, and Pt concentrations in the nanoparticle dispersions. 10 μ L of a nanoparticle dispersion was dissolved in concentrated nitric acid (955 μ L) and diluted with 3 mL water to determine Ag. 10 μ L of nanoparticle dispersion was dissolved in *aqua regia* (950 μ L) and diluted with 3 mL water to determine Au and Pt. The concentrations of Ag, Au, Pt, and S were determined by inductively coupled plasma mass spectrometry (Spectro model Spectro Arcos after microwave digestion) at Mikroanalytik-Labor Kolbe (Oberhausen, Germany).

2.9. Differential Centrifugal Sedimentation (DCS)

Differential centrifugal sedimentation, also known as analytical disc centrifugation, was performed with a CPS Instruments DC 24000 disc centrifuge (24,000 rpm, 29,000 relative centrifugal force; rcf). Different sucrose solutions (8 and 24 wt%) were used to obtain a density gradient. Dodecane (0.5 mL) was added as a top layer to prevent evaporation. Before each measurement, a dispersion of polyvinylchloride (PVC) latex in water with a specific hydrodynamic diameter of 483 nm by CPS was used for calibration. A volume of 100 μ L was added to the nanoparticle dispersion. For the calculation of the hydrodynamic diameter of the monometallic nanoparticles, the densities of elemental silver (10.49 g cm $^{-3}$), elemental platinum (21.45 g cm $^{-3}$), and elemental gold (19.32 g cm $^{-3}$) were used. For the bimetallic nanoparticles, the densities of elemental silver and elemental platinum were used according to the molar ratio of the particles.

2.10. UV-Vis Spectroscopy

UV-Vis spectroscopy was performed with water-dispersed nanoparticles from 200 nm to 800 nm (600 μ L sample volume) with a Genesis 50 instrument (ThermoFisher, Schwerte, Germany). Background correction was performed with ultrapure water as reference.

2.11. Fluorescence Spectroscopy

The fluorescence spectra were measured with water-dispersed nanoparticles on a Cary Eclipse spectrometer (Agilent Technologies, Santa Clara, CA, USA) in a fluorescence cuvette (600 μ L sample volume).

2.12. Synthesis of Glutathione-Coated Nanoparticles

The syntheses of glutathione-coated monometallic gold, platinum, and silver nanoparticles and of bimetallic Ag₅₀Pt₅₀ nanoparticles were reported earlier [30]. The synthesis

of Ag₇₀Pt₃₀ and Ag₂₀Pt₈₀ nanoparticles was carried out in the same way as with Ag₅₀Pt₅₀ particles by changing the ratio of silver to platinum and adjusting the reaction conditions. However, we found that the ratio of the elements found in the nanoparticles was not the same as the ratio of the elements in the precursor solution; i.e., silver was incorporated more easily than platinum into the bimetallic nanoparticles. With a series of experiments with different metal ratios, followed by elemental analysis of the bimetallic nanoparticles, the synthesis parameters were optimized.

To synthesize bimetallic Ag₂₀Pt₈₀ nanoparticles, 400 mL water was added to a 1 L round-bottomed flask. The water was degassed for 15 min with argon. Then, 450 µL of 100 mM silver nitrate solution (4.5 µmol, 0.5 mg Ag) and 4.1 mg glutathione (85.5 µmol) dissolved in 1 mL water were added. The solution was stirred for 30 min. Next, 445 µL H₂PtCl₆ ($c(\text{Pt}) = 37.5 \text{ g L}^{-1}$, 85.5 µmol, 16.7 mg Pt) and 26.0 mg glutathione (85.5 µmol) dissolved in 1 mL water were added and again stirred for 30 min. After that, 83.3 mg NaBH₄ (2.2 mmol) dissolved in 2 mL ice-cold water was quickly added. The stirring was continued for 30 min. The final dispersion had a brown color. Most of the water was removed under vacuum in a rotary evaporator. The Ag₂₀Pt₈₀ nanoparticles were isolated by spin filtration (10 kDa Amicon spin filters at 4000 rpm, 2500 × g, 20 min). They were then washed twice with 0.1 M NaOH and six times with water to remove unbound GSH and synthesis by-products. As determined with AAS, the yields were 90% (0.44 mg, 4.05 µmol) for silver and 21% (3.45 mg, 17.66 µmol) for platinum. With ICP-MS, the yields were 81% (0.39 mg, 3.65 µmol) for silver and 23% (3.83 mg, 19.6 µmol) for platinum. The molar ratio in the particles was 19% Ag to 81% Pt according to AAS and 16% Ag to 84% Pt according to ICP-MS.

To synthesize bimetallic Ag₇₀Pt₃₀ nanoparticles, 400 mL water was added to a 1 L round-bottomed flask. The water was degassed for 15 min with argon. Then, 2.25 mL of 200 mM silver nitrate solution (45 µmol, 4.85 mg Ag) and 40.5 mg glutathione (135 µmol) dissolved in 1 mL water were added. The solution was stirred for 30 min. Next, 234 µL H₂PtCl₆ ($c(\text{Pt}) = 37.5 \text{ g L}^{-1}$, 45 µmol, 8.78 mg Pt) and 13.9 mg glutathione (45 µmol) dissolved in 1 mL water were added and again stirred for 30 min. After that, 76 mg NaBH₄ (2.0 mmol) dissolved in 2 mL ice-cold water was quickly added. The stirring continued for 30 min. The final dispersion had a brown color. Most of the water was removed under vacuum in a rotary evaporator. The Ag₇₀Pt₃₀ nanoparticles were isolated by spin filtration (10 kDa Amicon spin filters at 4000 rpm, 2500 × g, 20 min). They were then washed twice with 0.1 M NaOH and six times with water to remove unbound GSH and synthesis by-products. AAS yields were 93% (4.53 mg, 42.0 µmol) for silver and 38% (3.29 mg, 16.9 µmol) for platinum. With ICP-MS, the yields were 96% (4.67 mg, 43.3 µmol) for silver and 39% (3.42 mg, 17.5 µmol) for platinum. The molar ratio in the particles was 71% Ag to 29% Pt according to AAS and 71% Ag to 29% Pt according to ICP-MS.

2.13. Fluorescent Labeling of GSH-Coated Nanoparticles

The surface azidation of the mono- and bimetallic GSH-coated nanoparticles was performed according to the procedure reported by Klein et al. [25] The click reaction of azide-containing nanoparticles with alkyne-terminated dyes was performed with a modified synthesis scheme reported by Klein et al. [25] and van der Meer et al. [35].

A stock solution of Cu-THPTA was prepared by mixing 2 mL CuSO₄ solution (5 mM, 10 µmol, 0.636 mg Cu), 2 mL saturated aminoguanidine solution, and 4 mL THPTA solution (48 mM, 192 µmol, 84 mg).

For the surface azidation of gold nanoparticles, Au-GSH nanoparticles (15 mg Au, 0.31 µmol NP) were dispersed in 18 mL water and 54 mL methanol in a 250 mL round-bottom flask for the surface azidation reaction. The azide transfer reagent imidazole-1-sulfonyl azide hydrogen sulfate (ISA; 184 mg, 676 µmol) was dissolved in 2 mL water and added to the reaction solution under vigorous stirring. Then, K₂CO₃ (94 mg, 676 µmol, dissolved in 2 mL water) was added to the reaction solution. The solution became cloudy and grayish after the addition of the reagents. Immediately thereafter, 1.04 mL of 5 mM

CuSO₄ solution (5.2 µmol) and 1 mL of 1 M NaOH were added. Water (about 20 mL) was then added until the turbidity had mostly disappeared. The solution was stirred at room temperature for 72 h. Prior to purification, the reaction solution was diluted to a total volume of 250 mL with water to keep the methanol content as low as possible for the subsequent spin filtration due to the sensitivity of the spin filters to organic solvents. The retrieved Au-N₃ particles were washed twice with 0.1 M NaOH and six times with water by spin filtration (10 kDa Amicon spin filter at 4000 rpm, 2500 × g, 20 min). The yield was 74% (11 mg Au) as determined by AAS.

For conjugation with AF647, Au-N₃ nanoparticles (62 nmol nanoparticles, 3 mg Au) were added to a 25 mL round bottom flask in 10 mL water. The solution was stirred and 100 µL 11.2 mM AF647-alkyne (1.12 µmol, 1 mg, 18 equivalents AF647 per nanoparticle) was added to the dispersion. Then 583 µL of the Cu-THPTA stock solution was added. Then 301 µL sodium ascorbate solution (10 mM, 3.6 µmol, 0.6 mg) was added to the nanoparticle dispersion. The reaction solution was stirred for 17 h at room temperature under light exclusion. Spin filtration was used for purification. Dispersions were centrifuged in Amicon 10 kDa spin filter at 4000 rpm, 2500 × g, for 20 min and washed with water until the filtrate was colorless (at least 12 times). The yield was 80% (2.4 mg Au) as determined by AAS.

The adapted synthesis conditions for the surface azidation and the click reaction for silver, platinum, and silver–platinum nanoparticles are summarized in Tables 1 and 2. All other conditions and parameters were the same as described here for gold nanoparticles.

Table 1. Reaction conditions for the synthesis of N₃-terminated nanoparticles (M-N₃). The nanoparticle concentration was computed assuming spherical nanoparticles of 2 nm diameter. All other synthesis conditions were the same as with gold nanoparticles. The yield was 50 to 90% with respect to the total metal content.

	Au	Ag	Ag ₅₀ Pt ₅₀	Pt
GSH-terminated nanoparticles used for the synthesis	15 mg Au, 0.31 µmol nanoparticles	15 mg Ag, 0.57 µmol nanoparticles	6.47 mg Ag, 11.7 mg Pt, 0.48 µmol nanoparticles	18.8 mg Pt, 0.35 µmol nanoparticles
round-bottomed flask	250 mL	500 mL	250 mL	250 mL
H ₂ O	18 mL	36 mL	20 mL	24 mL
methanol	54 mL	108 mL	60 mL	72 mL
ISA	184 mg, 676 µmol	394 mg, 1.45 mmol	221 mg, 812 µmol	357 mg, 1.31 mmol
K ₂ CO ₃	94 mg, 676 µmol	201 mg, 1.45 mmol	113 mg, 812 µmol	183 mg, 1.31 mmol
5 mM CuSO ₄ solution	1.04 mL, 5.2 µmol	2.52 mL, 12.6 µmol	3.67 mL, 18.4 µmol	3.91 mL, 19.6 µmol
1 M NaOH solution	1 mL	2 mL	2 mL	4 mL
Reaction time	72 h	48 h	48 h	72 h

Table 2. Reaction conditions for the synthesis of AF647-terminated nanoparticles (M-AF647). The nanoparticle concentration was computed assuming spherical nanoparticles of 2 nm diameter. All other synthesis conditions were the same as with gold nanoparticles. The yield was about 80% with respect to the total metal content.

	Au	Ag	Ag ₅₀ Pt ₅₀	Pt
N ₃ -terminated nanoparticles used for the synthesis	3 mg Au, 62 nmol nanoparticles	2.54 mg Ag, 96 nmol nanoparticles	1.85 mg Pt, 0.61 mg Ag, 61 nmol nanoparticles	3.7 mg Pt, 68 nmol nanoparticles
11.2 mM AF647-alkyne solution	100 µL, 1.12 µmol, 1 mg	155 µL, 1.73 µmol, 1.54 mg	100 µL, 1.12 µmol, 1 mg	61 µL, 0.68 µmol, 0.61 mg
Cu-THPTA solution	583 µL	853 µL	459 µL	1.5 mL
10 mM sodium ascorbate solution	301 µL, 3.6 µmol, 0.6 mg	246 µL, 2.46 µmol, 0.49 mg	164 µL, 1.6 µmol, 0.33 mg	535 µL, 5.4 µmol, 1.06 mg
Reaction time	17 h	6 h	17 h	17 h

2.14. Uptake of M-AF647 Nanoparticles by HeLa Cells

HeLa cells (obtained from American Type Culture Collection, ATCC, Manassas, USA) were cultured at 37 °C in 5% CO₂ in Gibco™ Dulbecco's modified Eagle's medium (DMEM), supplemented with 10% fetal bovine serum (FBS, obtained from ThermoFisher),

100 U mL⁻¹ penicillin, 100 U mL⁻¹ streptomycin, 1 mM Gibco™ sodium pyruvate, and 1 mM Gibco™ GlutaMAX. After a confluence of 70–90% was reached (after two to three days), the cells were passaged by trypsinization with 0.05% Gibco™ Trypsin-EDTA. Between each step of the experiment, the cells were washed three times with Gibco™ Dulbecco's buffered saline (DPBS).

The uptake of AF647-terminated ultrasmall nanoparticles by HeLa cells was analyzed in an 8-well chamber polymer slide surface modified with ibiTreat for tissue culture applications (μ-Slide 8-well, ibidi) by multiple focal plane confocal laser scanning microscopy (CLSM; TCS SP8X Falcon instrument from Leica Microsystems with a 63×/1.2 water immersion objective). Briefly, 2·10⁵ cells were seeded per well and incubated with 0.2 mL DMEM overnight at 37 °C in 5% CO₂ atmosphere. Finally, the cells were incubated with AF647-terminated nanoparticles at a concentration of 12.5 μg mL⁻¹ (metal content) nanoparticles per well. HeLa cells cultured in medium alone served as control group. After incubation for 24 h, the cells were washed three times with DPBS and fixed with a 4 vol% formaldehyde solution, according to standard protocols. The actin cytoskeleton of the cells was stained with AlexaFluor-448 phalloidin. Cell nuclei were stained with DAPI. Excitation wavelengths were 405 nm for DAPI (emission: 420 to 460 nm), 488 nm for AlexaFluor-488 (emission: 495 to 515 nm), and 647 nm for AF647 (emission: 660 to 700 nm). For the CLSM images, z-stacks were taken across the cells at a distance of 200 nm. All nanoparticles were investigated after four weeks of storage in dispersion.

2.15. MTT Tests of M-GSH Nanoparticles with HeLa Cells

The cell viability after nanoparticle incubation was determined with an MTT assay. HeLa cells were first seeded at a density of 20,000 cells per well in a 24-well plate and then incubated with 0.5 mL DMEM overnight at 37 °C and 5% CO₂ atmosphere. The cells were then incubated with GSH-terminated nanoparticles. The dispersions of the nanoparticles were tested at concentrations between 2.5 μg mL⁻¹ and 100 μg mL⁻¹ (metal content). HeLa cells cultured in medium served as control. After the cells had been incubated for 24 h, they were washed three times with DPBS to remove the nanoparticles. To prepare the staining solution, 30 mg MTT was dissolved in 5 mL DPBS and diluted with 25 mL DMEM to a final concentration of 1 mg mL⁻¹. To each well, 0.3 mL of the staining solution was added, and the cells were incubated for 1 h at 37 °C and 5% CO₂ atmosphere. The solution was removed and 0.3 mL of DMSO was added into each well and incubated for 30 min at room temperature. The amount of dissolved formazan was quantified in a 96-well plate with a Multiscan plate reader (Thermo Fisher, Schwerte, Germany) at 570 nm. For each nanoparticle type and concentration, at least two independent cell culture experiments were performed. All nanoparticles were investigated after four weeks of storage in dispersion.

2.16. Antibacterial Tests of M-GSH Nanoparticles with *Staphylococcus xylosus* and *Escherichia coli*

The minimal inhibitory concentration (MIC) is defined as the lowest concentration of an antimicrobial agent or drug that inhibits the growth of a given microbial strain in vitro. Bacterial strains were cultivated in Lysogeny Broth (LB, 20 g L⁻¹) and Trypticase Soy Broth (TSB). TSB was prepared by mixing CASO-Bouillon (30 g L⁻¹) and yeast extract (3 g L⁻¹). To prepare solid media, Agar-Agar Kobe I was added to liquid media (15 g L⁻¹). All reagents for media preparation were purchased from Carl Roth. The culture media were sterilized by autoclaving (LABOKLAV 25, SHP Steriltechnik, Detzel Schloß, Germany). Liquid cultures of *Staphylococcus xylosus* DSM 6179 (Schleifer and Kloos 1975) and *Escherichia coli* DH5α were grown overnight (130 rpm, 37 °C) in a MaxQ™ 4000 orbital shaker (Thermo Scientific, USA). Next, log-phase liquid cultures of bacteria were prepared by inoculating (5% v/v) sterile TSB and LB culture media from overnight cultures of *S. xylosus* and *E. coli*, respectively. Bacteria were grown (180 rpm, 37 °C) until the fresh cultures had reached an optical density of 0.6 at the wavelength of 600 nm (cell density meter WPA Biowave, Thermo Fisher, Schwerte, Germany), which indicates the logarithmic growth phase of the bacterial cultures.

MIC experiments were performed in 96-well microplates (Thermo Fisher, Schwerte, Germany). Briefly, 190 μL of M-GSH nanoparticle-containing culture medium per well was mixed with 10 μL of the appropriate bacterial log-phase culture. The plate was then incubated overnight with gentle rotation in an orbital shaker (90 rpm, 37 °C). The MIC values were determined spectrophotometrically after 24 h of incubation with a HiPo MPP-96 microplate reader (Biosan, Riga, Latvia) at a wavelength of 620 nm. Each sample was prepared and measured in triplicate. As reference, media supplemented with dissolved AgNO_3 as source of cytotoxic silver ions were investigated. The range of 0–100 $\mu\text{g mL}^{-1}$ nanoparticles/salt was studied in steps of 0, 5, 10, 15, 25, 50, 75, and 100 $\mu\text{g metal mL}^{-1}$. Parallel to the MIC experiments, CFU (colony-forming unit) values of the log-phase cultures were determined on agar plates after overnight incubation at 37 °C (HerathermTM Compact, Thermo Fisher, Schwerte, Germany) to determine culture viability and bacterial cell dose per well. Bacterial colonies were counted with an SC6+ digital colony counter (VWR International, Darmstadt, Germany). All nanoparticles were investigated after four weeks of storage in dispersion.

3. Results

The syntheses and physico-chemical characterization data of monometallic glutathione-coated gold, silver, and platinum nanoparticles, as well as $\text{Ag}_{50}\text{Pt}_{50}$ nanoparticles, were reported earlier [30]. Bimetallic nanoparticles with the compositions of $\text{Ag}_{70}\text{Pt}_{30}$ and $\text{Ag}_{20}\text{Pt}_{80}$ were prepared in addition to assess the effect of the metal ratio in the nanoalloys. All particles were synthesized by reduction of the corresponding metal salts with NaBH_4 in a modified Brust–Schiffrin synthesis with glutathione (GSH) as stabilizing ligand [36–39]. The characterization data of the additional bimetallic compositions $\text{Ag}_{70}\text{Pt}_{30}$ and $\text{Ag}_{20}\text{Pt}_{80}$ were well in line with the other mono- and bimetallic particles.

HRTEM images of the GSH-coated nanoparticles are shown in Figure 1. The average particle diameter was about 2 nm. Electron diffraction accompanied by Fast Fourier Transform (FFT) indicated amorphous $\text{Ag}_{70}\text{Pt}_{30}$ and crystalline $\text{Ag}_{20}\text{Pt}_{80}$ particles in agreement with amorphous $\text{Ag}_{50}\text{Pt}_{50}$ nanoparticles [30]. The monometallic Ag, Au, and Pt nanoparticles were all crystalline, as shown earlier by electron diffraction [30].

The hydrodynamic diameter of the nanoparticles dispersed in water was determined with differential centrifugal sedimentation (DCS; Figure S1). The diameter of the dispersed $\text{Ag}_{70}\text{Pt}_{30}$ and $\text{Ag}_{20}\text{Pt}_{80}$ nanoparticles was less than 2 nm, indicating a good dispersibility in water without detectable agglomeration. This was confirmed by dynamic light scattering (DLS) that did not give a scattering signal. Note that DCS generally underestimates the particle size because the actual density of the particles is lower due to the hydrated ligand shell [40].

Small-angle X-ray scattering showed well-dispersed nanoparticles (Figure S2). From the data analysis, a diameter of 1.0 ± 0.1 nm with polydispersities of 0.4 nm and 0.5 nm for $\text{Ag}_{70}\text{Pt}_{30}$ and $\text{Ag}_{20}\text{Pt}_{80}$, respectively, was obtained. Moderate particle interactions were observed, giving a hard sphere radius of 3.5 ± 0.1 nm and a volume fraction of 0.054 ± 0.005 for $\text{Ag}_{70}\text{Pt}_{30}$ nanoparticles. The corresponding values for $\text{Ag}_{20}\text{Pt}_{80}$ nanoparticles were 4.1 ± 0.1 nm and 0.071 ± 0.006 . X-ray powder diffraction indicated very small particles, as shown by the very broad diffraction peaks with indications for the presence of oxidized silver (Figure S3). X-ray photoelectron spectroscopy confirmed the oxidized nature of the particles which was also detected earlier in $\text{Ag}_{50}\text{Pt}_{50}$ nanoparticles [30]. Silver was fully oxidized, and platinum was present as a mixture of metallic platinum and oxidized platinum species (Figure S4). NMR spectroscopy, which is possible for ultrasmall nanoparticles [41], showed the firm attachment of glutathione to the nanoparticles and the absence of free (dissolved) glutathione (Figures S5–S9). The hydrodynamic diameter of the dispersed particles, together with the ligand shell, was probed with ^1H -DOSY-NMR spectroscopy. The number of glutathione ligands on the surface of each nanoparticle was determined to be 200 to 300 with ICP-MS (see ref. [30] and Table 3 for detailed stoichiometric and analytical data).

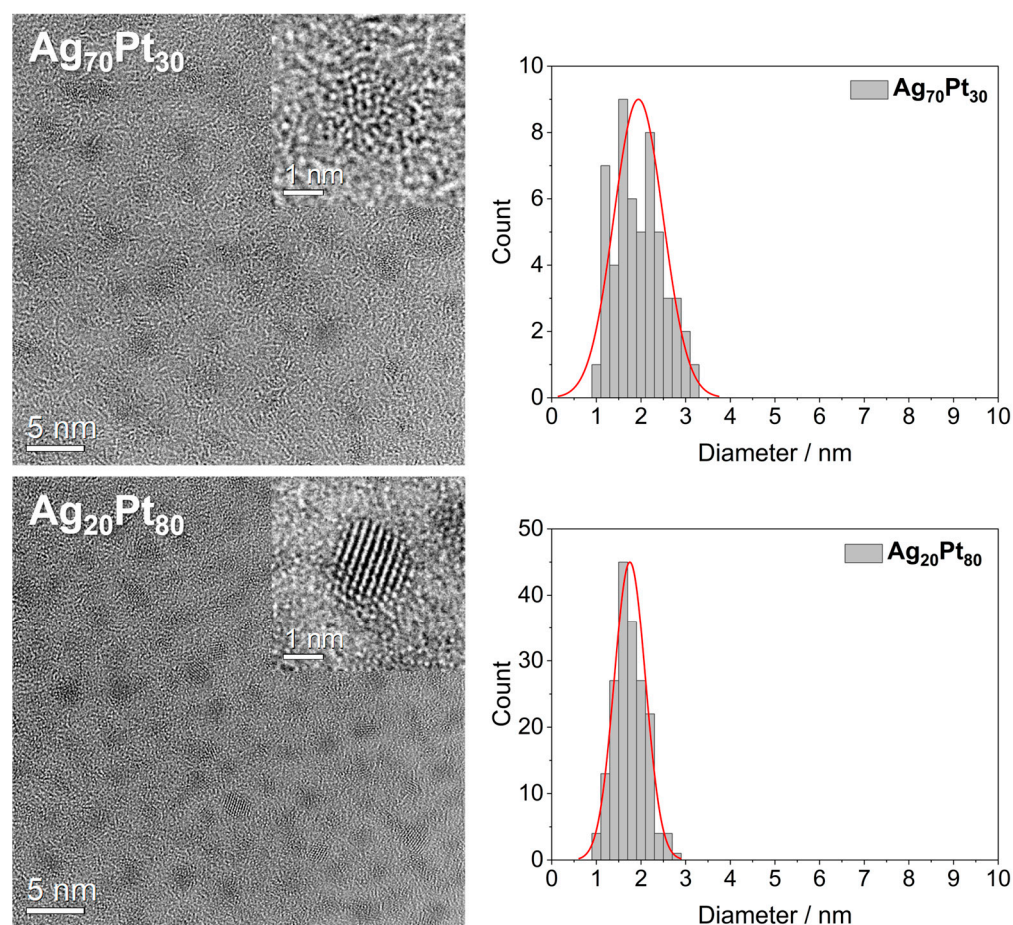


Figure 1. HRTEM images of GSH-coated $\text{Ag}_{70}\text{Pt}_{30}$ and $\text{Ag}_{20}\text{Pt}_{80}$ bimetallic nanoparticles, together with manually determined particle size distributions (red: fit line). A magnified particle is shown in the upper right corner of each overview image. $\text{Ag}_{70}\text{Pt}_{30}$ particles were amorphous and $\text{Ag}_{20}\text{Pt}_{80}$ particles were crystalline. Note the higher contrast of the Pt-rich nanoparticles due to the heavier Pt atoms.

Monometallic gold, silver, and platinum nanoparticles, as well as bimetallic $\text{Ag}_{50}\text{Pt}_{50}$ nanoparticles, were surface-conjugated with the fluorescent dye AlexaFluor-647 (AF647) as reported earlier for gold nanoparticles [25]. The reaction procedure is schematically depicted in Figure 2, i.e., first the synthesis of M-GSH nanoparticles, followed by surface azidation to M- N_3 nanoparticles [25], and finally conjugation of the alkyne-terminated dye AF647 via copper-catalyzed azide-alkyne cycloaddition (CuAAC) to yield M-AF647 nanoparticles [42]. This fluorescent labeling permits us to trace the particles during cell culture experiments. The particle types $\text{Ag}_{70}\text{Pt}_{30}$ and $\text{Ag}_{20}\text{Pt}_{80}$ were not fluorescently labeled as their uptake by cells is not expected to be different from Au, Ag, Pt, and $\text{Ag}_{50}\text{Pt}_{50}$ nanoparticles (same size, just different metal cores).

With a combination of UV-Vis spectroscopy (giving the concentration of AF647) and atomic absorption spectroscopy (AAS; giving the concentration of gold nanoparticles), between 6 and 13 AF647 molecules were detected on each nanoparticle (see Table 3), in good agreement with earlier data on dye-conjugated ultrasmall gold nanoparticles [25,35,43].

Figure 3 shows fluorescence spectra of all labeled M-AF647 nanoparticles. All particles showed a distinct fluorescence, demonstrating that no significant quenching occurred as expected for ultrasmall nanoparticles [44].

Confocal laser scanning microscopy was used to follow the uptake of the fluorescently labeled M-AF647 nanoparticles by HeLa cells (Figure 4). All particles were well taken up by the cells.

To assess the cytotoxicity of GSH-coated ultrasmall nanoparticles, an MTT assay with HeLa cells was performed (Figure 5 and Table 4). This assay provides information on

the metabolic activity of the cells and serves as an indicator of cell viability and proliferation [45]. In addition to monometallic and bimetallic silver–platinum nanoparticles, a physical mixture of the monometallic nanoparticles was also used to investigate possible polarization effects. All viability data were normalized to untreated cells (100%). Cell viabilities above 100% in some cases are considered not significant and within the experimental error.

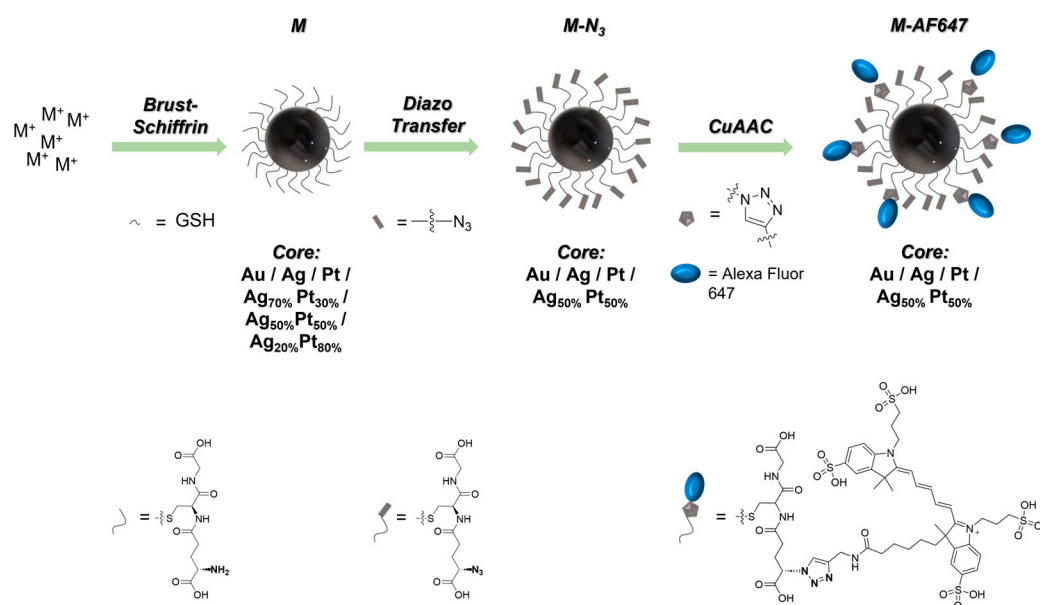


Figure 2. Synthetic pathway of the synthesis and the covalent attachment of AF647 molecules to the surface of ultrasmall GSH-coated nanoparticles.

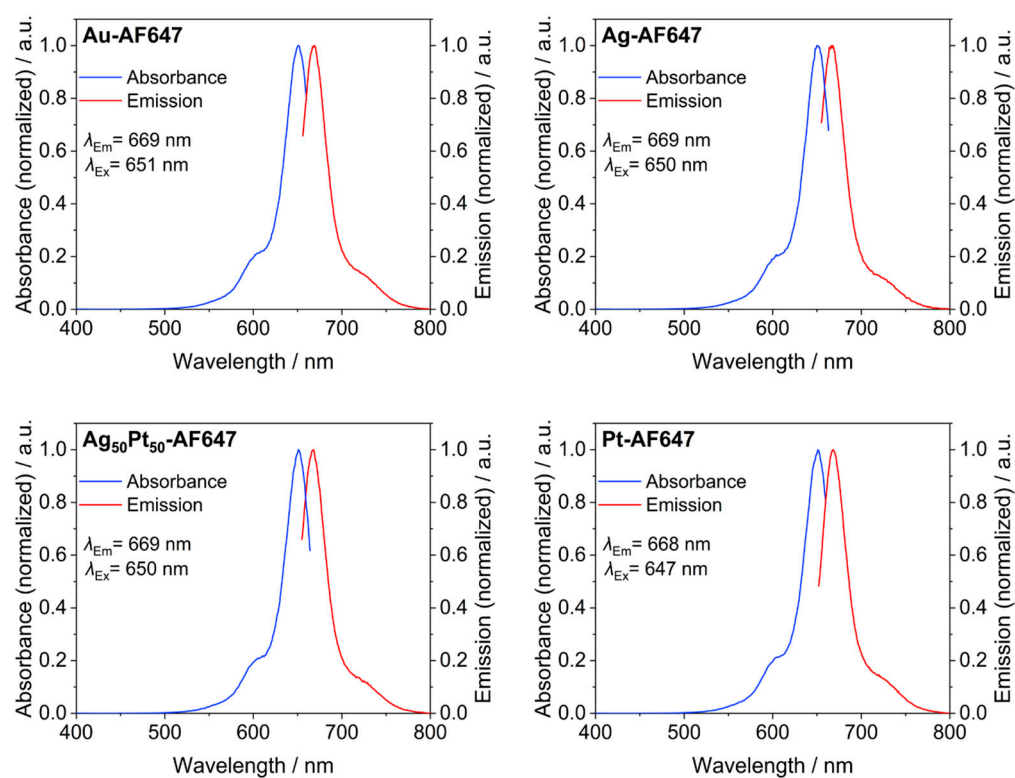


Figure 3. Normalized fluorescence spectra of M-AF647 nanoparticles. Absorption spectra (blue) and emission spectra (red) are shown.

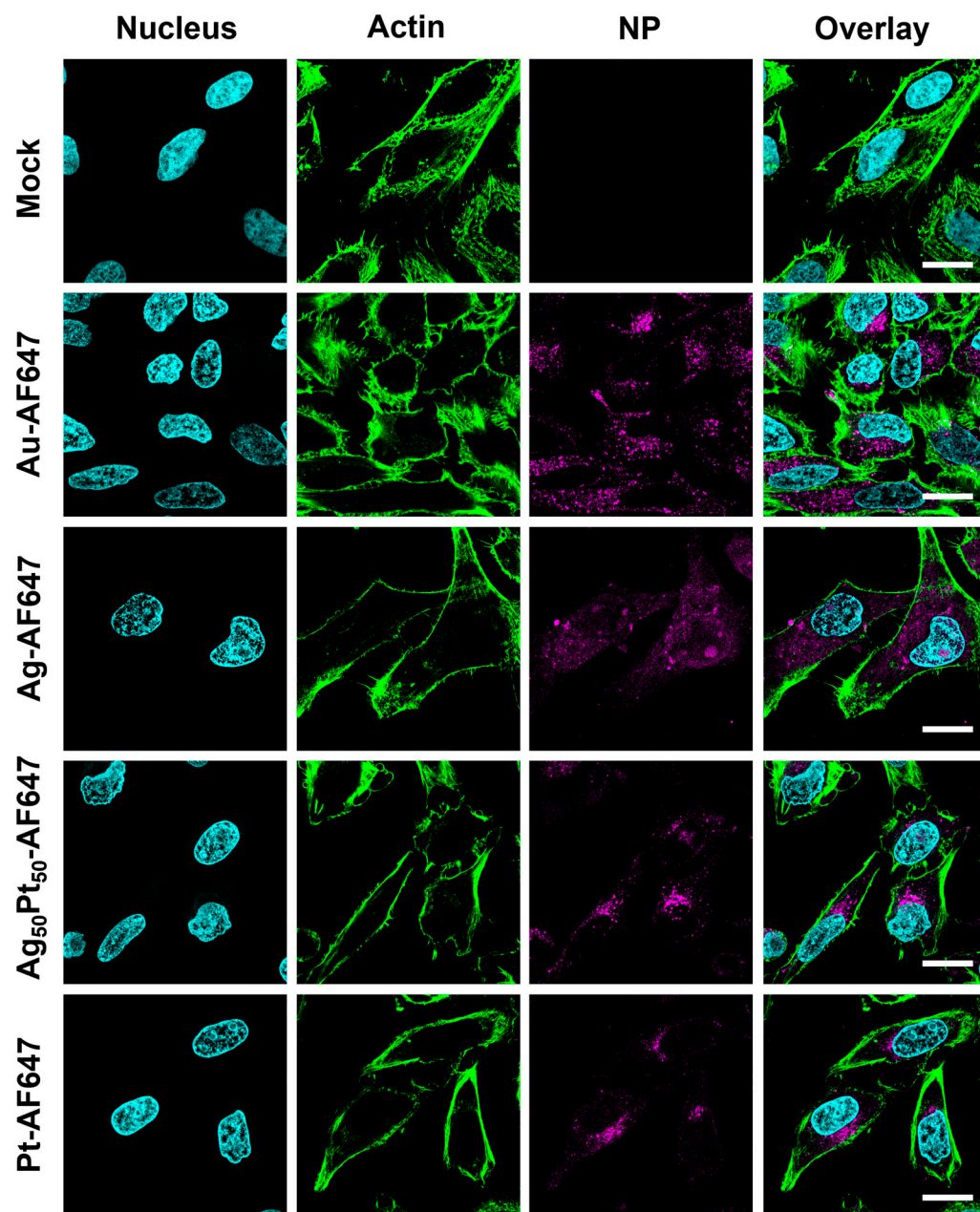


Figure 4. Confocal laser scanning images showing the uptake of ultras-small AF647-functionalized nanoparticles. HeLa cells were incubated with $12.5 \mu\text{g mL}^{-1}$ nanoparticles (metal concentration) for 24 h, followed by washing, fixation, and staining. **Mock:** Untreated HeLa cells (no nanoparticles). **Nuclei:** DAPI staining (blue). **Actin:** staining with AlexaFluor™-488 phalloidin (green). **NP:** AF647 fluorescence, showing the nanoparticles (magenta). All scale bars are $20 \mu\text{m}$.

The antibacterial activity of the GSH-coated nanoparticles was assessed by determination of the minimal inhibitory concentration (MIC) in broth cultures of Gram-negative (G-) *Escherichia coli* and Gram-positive (G+) *Staphylococcus xylosus* bacteria (Table 5). MIC values of monometallic nanoparticles (Ag, Au, and Pt) were above the highest studied nanoparticle concentration ($100 \mu\text{g mL}^{-1}$). In other words, the particles were not toxic for both bacterial strains. MIC values of the bimetallic nanoparticles ($\text{Ag}_{50}\text{Pt}_{50}$) ranged from $1\text{--}5 \mu\text{g mL}^{-1}$ for *S. xylosus* to $11\text{--}15 \mu\text{g mL}^{-1}$ for *E. coli*, indicating a significant cytotoxic effect against bacteria, especially towards Gram-positive *S. xylosus*. These concentrations are in the range that is characteristic for potent conventional antibiotics [46–48]. In contrast,

the incubation with a physical mixture of monometallic nanoparticles (Ag/Pt 50:50) gave MIC results comparable to the monometallic nanoparticles, i.e., a low cytotoxicity.

Table 3. Analytical data of all prepared and investigated GSH-coated ultrasmall nanoparticles.

	Ag	Ag ₇₀ Pt ₃₀	Ag ₅₀ Pt ₅₀	Ag ₂₀ Pt ₈₀	Pt	Au
particle core volume/nm ³	4.19 *	4.19 *	4.19 *	4.19 *	4.19 *	4.19 *
particle core weight/g·10 ²³	4.39 *	5.54 *	6.69 *	7.84 *	8.98 *	8.09 *
particle density/g cm ⁻³	10.49	13.78 **	15.97 **	19.26 **	21.45	19.32
particle core surface area/nm ²	12.57 *	12.57 *	12.57 *	12.57 *	12.57 *	12.57 *
hydrodynamic diameter (DCS)/nm	1.7 ± 0.5 ***	1.5 ± 0.3	1.6 ± 0.3 ***	1.6 ± 0.4	1.6 ± 0.4 ***	1.5 ± 0.3 ***
diffusion coefficient (¹ H-DOSY)/10 ⁻¹⁰ m ² s ⁻¹	1.47 ***	1.53	1.60 ***	1.69	1.56 ***	1.28 ***
hydrodynamic diameter (¹ H-DOSY)/nm	3.32 ***	3.19	3.05 ***	2.88	3.14 ***	3.81 ***
particle core diameter (HRTEM)/nm	2.2 ± 0.5 ***	1.9 ± 0.6	1.8 ± 0.4 ***	1.8 ± 0.3	2.0 ± 0.4 ***	2.0 ± 0.4 ***
particle core diameter (SAXS)/nm	1.0 ± 0.1 ***	1.0 ± 0.1	1.6 ± 0.1 ***	1.0 ± 0.1	0.9 ± 0.1 ***	0.8 ± 0.2
crystallinity by TEM	crystalline ***	amorphous	amorphous ***	crystalline	crystalline ***	crystalline ***
oxidation state of metals by XPS	Ag ⁺ ***	Ag ⁺ , Pt, Pt ²⁺	Ag ⁺ , Pt, Pt ²⁺ ***	Ag ⁺ , Pt, Pt ²⁺	Pt, Pt ²⁺ ***	Au ***
normalized molar ratio metal(M):sulfur(S) by ICP-MS	1.00 (Ag):1.28 (S) ***	0.71 (Ag):0.29 (Pt):0.65 (S)	0.59 (Ag):0.41 (Pt):0.68 (S) ***	0.16 (Ag):0.84 (Pt):1.35 (S)	1.00 (Pt):0.73 (S) ***	1.00 (Au):0.82 (S) ***
overall nominal composition of one nanoparticle	Ag ₂₄₅ GSH ₃₁₅ ***	Ag ₁₈₄ Pt ₇₄ GSH ₁₇₀	Ag ₁₅₆ Pt ₁₁₀ GSH ₁₈₀ ***	Ag ₄₃ Pt ₂₃₀ GSH ₃₇₀	Pt ₂₇₇ GSH ₂₀₆ ***	Au ₂₄₇ GSH ₂₀₃ ***
GSH molecular footprint/nm ²	0.040 ***	0.074	0.070 ***	0.034	0.062 ***	0.062 ***
number of conjugated AlexaFluor-647 molecules on each M-AF647 nanoparticle by AAS and UV-VIS	13	-	8	-	6	12

*: Computed values based on the assumption that the average particle diameter was 2 nm and that the nanoparticles were spherical. ** Computed from the stoichiometry as determined with ICP-MS. *** The data of GSH-coated Ag, Au, Pt, and Ag₅₀Pt₅₀ nanoparticles were taken from ref. [30].

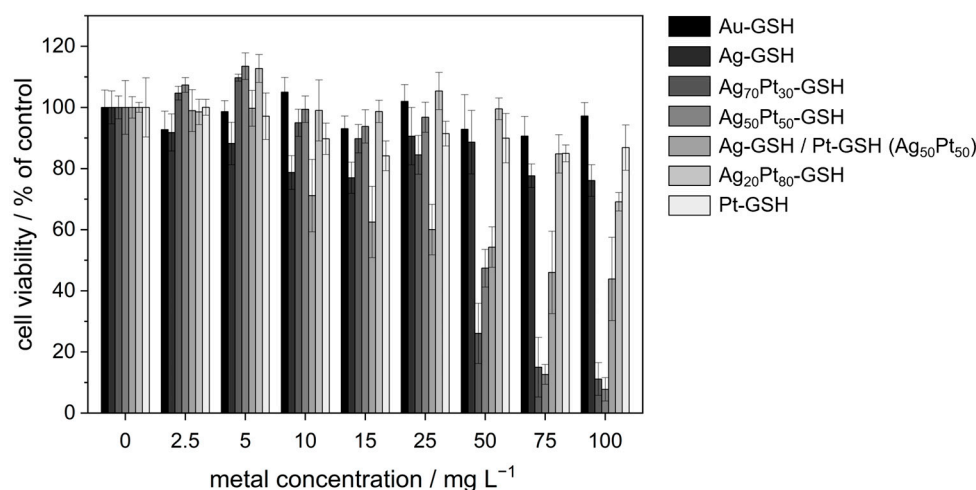


Figure 5. MTT viability assay carried out with HeLa cells after incubation for 24 h with water-dispersed GSH-coated nanoparticles. For the bimetallic silver nanoparticles, the given concentrations refer to the total metal concentration. Ag/Pt (50:50) represents an equimolar 50:50 physical mixture of Ag and Pt nanoparticles. The data represent the mean of two individual experiments with the error bars indicating the standard deviation ($N = 2$).

It is now well accepted that silver nanoparticles dissolve over time under the release of cytotoxic silver ions [49–53]. The presence of dissolved oxygen is necessary for the oxidation and subsequent dissolution of silver that causes the toxic effect [54–59]. Therefore, we studied the release of silver ions from ultrasmall nanoparticles by filtration experiments through spin filters (3 kDa). The nanoparticles were incubated in water in closed vessels

but without degassing at 4 °C, 25 °C, and 37 °C for up to 14 days and then separated from released silver ions by spin filtration. The filtrate was analyzed by AAS for silver ions. The procedure was validated with the analysis of a solution of silver nitrate (full permeation through the spin filter), a dispersion of gold nanoparticles (GSH-coated; 2 nm; no permeation through the spin filter), and as control a mixture of dissolved silver nitrate and dispersed gold nanoparticles. This gave the expected results, i.e., Ag⁺ ions went through the filter and gold nanoparticles were restrained. Only very small amounts of silver ions were detected for the Ag and Ag₅₀Pt₅₀ nanoparticles, irrespective of storage time and temperature (Figure 6). In other words, no significant dissolution of the nanoparticles was detected for monometallic and bimetallic silver nanoparticles.

Table 4. Cell viabilities (in %) by the MTT test of GSH-coated nanoparticles as function of the total metal content $c(\text{metal})$ (mean \pm standard deviation in percent). For silver-containing particles, the effective silver concentration is given in parentheses in $\mu\text{g mL}^{-1}$.

$c(\text{Metal})/\text{in } \mu\text{g mL}^{-1}$	Au	Ag	Ag ₇₀ Pt ₃₀	Ag ₅₀ Pt ₅₀	Ag/Pt (50:50)	Ag ₂₀ Pt ₈₀	Pt
0	100 \pm 6	100 \pm 5 (Ag: 0)	100 \pm 4 (Ag: 0)	100 \pm 9 (Ag: 0)	100 \pm 4 (Ag: 0)	100 \pm 2 (Ag: 0)	100 \pm 10
2.5	93 \pm 6	92 \pm 6 (Ag: 2.5)	105 \pm 2 (Ag: 1)	107 \pm 2 (Ag: 0.9)	99 \pm 7 (Ag: 0.9)	98 \pm 4 (Ag: 0)	100 \pm 3
5	99 \pm 4	88 \pm 7 (Ag: 5)	110 \pm 1 (Ag: 2.8)	114 \pm 4 (Ag: 1.8)	100 \pm 6 (Ag: 1.8)	113 \pm 5 (Ag: 0.6)	97 \pm 8
10	105 \pm 5	79 \pm 6 (Ag: 10)	95 \pm 4 (Ag: 5.6)	99 \pm 4 (Ag: 3.6)	71 \pm 12 (Ag: 3.6)	99 \pm 10 (Ag: 1)	90 \pm 5
15	93 \pm 4	77 \pm 5 (Ag: 15)	90 \pm 5 (Ag: 8.5)	94 \pm 5 (Ag: 5)	62 \pm 12 (Ag: 5)	99 \pm 4 (Ag: 1.8)	84 \pm 5
25	102 \pm 6	91 \pm 9 (Ag: 25)	84 \pm 6 (Ag: 14)	97 \pm 5 (Ag: 8.9)	60 \pm 8 (Ag: 8.9)	105 \pm 6 (Ag: 3)	91 \pm 4
50	93 \pm 11	89 \pm 10 (Ag: 50)	26 \pm 10 (Ag: 28)	47 \pm 6 (Ag: 18)	54 \pm 7 (Ag: 18)	100 \pm 4 (Ag: 6)	90 \pm 8
75	91 \pm 6	78 \pm 4 (Ag: 75)	15 \pm 10 (Ag: 42)	13 \pm 3 (Ag: 27)	46 \pm 14 (Ag: 27)	85 \pm 6 (Ag: 9)	85 \pm 3
100	97 \pm 4	76 \pm 5 (Ag: 100)	11 \pm 5 (Ag: 56)	8 \pm 4 (Ag: 36)	44 \pm 14 (Ag: 36)	69 \pm 3 (Ag: 12)	87 \pm 7

Table 5. MIC values determined for *E. coli* DH5 α and *S. xyloso* DSM 6179 after 24 h of incubation with different doses of GSH-coated nanoparticles, given in $\mu\text{g mL}^{-1}$ (metal content). The effective silver concentration is given in parentheses in $\mu\text{g mL}^{-1}$, where appropriate. *E. coli* (CFU: $1.1 \cdot 10^8$ cells mL^{-1} ; cell dose: $1.1 \cdot 10^6$ cells per well), *S. xyloso* (CFU: $5 \cdot 10^7$ cells mL^{-1} ; cell dose: $5 \cdot 10^5$ cells per well).

Sample	<i>E. coli</i> (Gram-Negative)	<i>S. xyloso</i> (Gram-Positive)
AgNO ₃	6–10 (6–10)	15–25 (15–25)
Ag	>100 (>100)	>100 (>100)
Au	>100 (–)	>100 (–)
Pt	>100 (–)	>100 (–)
Ag ₅₀ Pt ₅₀	11–15 (4–5.4)	1–5 (0.4–1.8)
Ag/Pt (50:50)	76–100 (27–36)	>100 (>36)

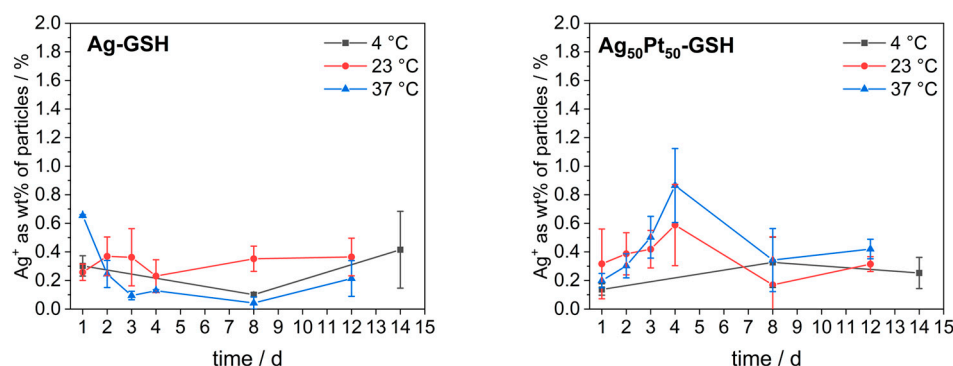


Figure 6. Dissolution of monometallic silver and bimetallic GSH-coated Ag₅₀Pt₅₀ nanoparticles stored in non-degassed pure water (i.e., in the presence of dissolved oxygen) at 4 °C, 25 °C, and 37 °C for up to 14 days.

4. Discussion

All nanoparticles had a uniform, mostly spherical shape and were well dispersible in water. Therefore, it is not surprising that they were easily taken up by HeLa cells. The nature of the metal core did not influence the uptake by cells or the intracellular localization; i.e., the interaction with cells was governed by their surface chemistry (e.g., the surface charge) [60]. The accumulation of the nanoparticles inside the cells suggests their presence inside endolysosomes [61]. However, the nanoparticles did not enter the cell nucleus (at least not to a significant extent), as sometimes reported for ultrasmall nanoparticles [35,62]. This is well in line with earlier observations on fluorescent ultrasmall nanoparticles. A size-dependent intracellular localization was reported for MCF7 breast cancer cells. Gold nanoparticles of 2 and 6 nm diameter were found in the nucleus, while their larger plasmonic analogues (10 and 16 nm) reached only the cytoplasm [62]. Yang et al. [63] and Carrillo-Carrion et al. [64] reported similar results for gold nanoparticles and quantum dots in the ultrasmall size range. Uptake studies of fluorescent ultrasmall gold nanoparticles (2 nm) in CT-26 cells to elucidate the uptake mechanism of ultrasmall nanoparticles were performed in the presence of various endocytosis inhibitors. It was shown that the uptake of the nanoparticles with CT-26 cells was not inhibited by a single endocytosis inhibitor. However, cooling to 4 °C led to a strong inhibition of the uptake. This excludes a purely diffusion-controlled migration across the cell membrane. Clearly, a combination of different endocytosis pathways is active for the uptake of ultrasmall nanoparticles [65].

Despite the considerable uptake by HeLa cells, we observed no significant toxic effect for ultrasmall gold and platinum nanoparticles, except at very high concentrations, well in line with their noble and inert nature. Ultrasmall gold nanoparticles were studied in depth regarding their cytotoxicity. For example, ultrasmall gold nanoparticles terminated with GSH (1.7 nm) were not cytotoxic for HeLa cells up to 32 µg gold mL⁻¹ [66]. Gold clusters were cytotoxic only below 2 nm size and only if the gold surface was accessible for biomolecules or cell constituents, which is the case for phosphane-ligand stabilized nanoparticles [67]. Rostek et al. prepared poly(N-vinylpyrrolidone) (PVP)-stabilized spherical gold, platinum, and silver nanoparticles with a size of 4 to 8 nm and incubated hMSC cells with them. Neither platinum nor gold nanoparticles had any effect on cell viability. Only silver nanoparticles showed a cytotoxic activity [68].

Surprisingly, monometallic ultrasmall silver nanoparticles showed a low cytotoxicity on HeLa cells and bacteria at all concentrations in our study. However, the effect was small as the release of silver ions was almost negligible. In general, the toxic concentration of silver is about 1–10 µg mL⁻¹ for silver ions and 10–100 µg mL⁻¹ for silver nanoparticles, depending on the cell type and the cultivation conditions [13]. For bacteria, it is of the order of 0.1 to 1 µg mL⁻¹ for silver ions and 0.1 to 1 µg mL⁻¹ for silver nanoparticles, depending on the bacterium, the culture conditions, and the type of nanoparticle [13]. For *Staphylococcus aureus*, larger silver nanoparticles of different size and shape (10 to 100 nm) were reported with a MIC of 25 to 50 µg mL⁻¹ [69]. In a comparative study, the toxic effect of silver administered as ions (silver acetate) occurred at 0.5 to 5 µg mL⁻¹ for *E. coli*, *S. aureus*, human mesenchymal stem cells (hMSCs), and peripheral blood mononuclear cells (PBMCs). PVP-stabilized silver nanoparticles (70 nm) gave a cytotoxic effect on the same bacteria and cells in the concentration range of 12.5 to 50 µg mL⁻¹ for silver nanoparticles [14]. It was also demonstrated a decade ago that silver chloride is immediately formed after release of silver ions from silver nanoparticles [70], and that silver nanoparticles are neither toxic to bacteria [71] nor to cells [58,71] in the absence of oxygen, i.e., without oxidative dissolution. In contrast, ultrasmall GSH-coated silver nanoparticles (2 nm) showed a remarkably high cytotoxicity where about 50% of HeLa cells were dead at a concentration of 15 µg mL⁻¹ after 3 h and at a concentration of 1 µg mL⁻¹ after 24 h. These nanoparticles were also easily taken up by HeLa cells within 24 h and found in the cytosol [72]. The difference to our study is probably the fact that the particles analyzed in our study were stored for 4 weeks in dispersion for aging.

It shall be noted that all particle characterization data (physico-chemical and biological) that are reported here were obtained with nanoparticles that were immersed in water at ambient temperature for four weeks. During the initial experiments, it turned out that the cytotoxicity towards cells and bacteria varied with the age of the particles in an erratic way, although their physico-chemical properties like particle size did not significantly change. After four weeks of storage, all data were consistent and reproducible. It is possible that the particles underwent an internal change during immersion in water that influenced their internal structure and their biological effects. This would also explain the much higher cytotoxicity observed for freshly prepared silver nanoparticles [72]. However, the elucidation of this effect would require extensive time-resolved studies that were beyond the scope of this study.

The cytotoxicity of the bimetallic silver-platinum nanoparticles was higher than that of monometallic silver nanoparticles, both for HeLa cells and bacteria. The critical concentrations for a 50% cytotoxicity for HeLa cells were about $50 \mu\text{g mL}^{-1}$ for $\text{Ag}_{70}\text{Pt}_{30}$ and $\text{Ag}_{50}\text{Pt}_{50}$ and $75 \mu\text{g mL}^{-1}$ for the physical mixture of Ag/Pt nanoparticles. A 50% cytotoxicity was not reached for Au, Ag, Pt, and $\text{Ag}_{20}\text{Pt}_{80}$ nanoparticles. Notably, $\text{Ag}_{50}\text{Pt}_{50}$ nanoparticles were significantly more cytotoxic than an equimolar physical mixture (50:50) of Ag and Pt nanoparticles [73]. The MIC values of bimetallic nanoparticles were close to or even lower than for silver nitrate, used in this study as reference and source of bactericidal silver ions. Thus, the bimetallic silver-platinum nanoparticles were more toxic against HeLa cells and bacteria than monometallic silver nanoparticles. This cannot be due to an enhanced release of silver ions as the bimetallic $\text{Ag}_{50}\text{Pt}_{50}$ nanoparticles did not dissolve in water.

Many of the available reports on studies on the antibacterial activity of bimetallic nanoparticles compared to their monometallic counterparts are based on the application of Au-Ag nanoparticles, but the mechanism of their bactericidal action remains not fully understood [74]. Little is known about the cytotoxicity of bimetallic silver-platinum nanoparticles so far. There is an ongoing discussion on a sacrificial anode effect in alloyed nanoparticles which could lead to polarization and an enhanced dissolution of cytotoxic silver ions. It has been shown theoretically that a noble metal can protect a less noble metal from oxidation [75]. On the other hand, a noble metal can enhance the dissolution rate by increasing the apparent charge of Ag^0 to Ag^+ by electrochemical polarization [76]. A potential sacrificial anode effect was reported for silver-platinum surface coatings [77–80]. Grasmik et al. prepared bimetallic AgPt nanoparticles of 15 to 25 nm diameter with PVP coating and found a cytotoxicity against hMSC above a silver content of 50 mol%, supported by silver-release experiments where silver was only released above 50 mol% silver [22]. Breisch et al. studied the antibacterial effects of a physical mixture of PVP-coated Ag and Pt nanoparticles (both 7 nm) against *E. coli* and *S. aureus* and observed an enhancement of the cytotoxicity of silver nanoparticles in the presence of platinum nanoparticles [73]. In contrast, alloyed nanoparticles (10 nm; PVP-coated) of the compositions Ag, $\text{Ag}_{10}\text{Pt}_{90}$, $\text{Ag}_{30}\text{Pt}_{70}$, $\text{Ag}_{50}\text{Pt}_{50}$, $\text{Ag}_{70}\text{Pt}_{30}$, $\text{Ag}_{90}\text{Pt}_{10}$, and Pt did not show an enhanced bactericidal effect [21]. Yang et al. prepared 2.1 nm bimetallic nanoparticles of Ag and Cu and reported a considerably enhanced silver release rate [81]. Singh et al. prepared bovine serum albumin (BSA)-capped bimetallic AgPt nanoparticles of 10 to 15 nm diameter but did not find an adverse effect on the viability and the morphology of human gingival fibroblasts exposed to the nanoparticles for 24 h. This was in sharp contrast to the precursor salts that released silver or platinum ions, i.e., Ag_2SO_4 and H_2PtCl_6 , respectively, suggesting that the surface of the nanoparticles was well blocked by attached thiol groups from the BSA. However, the authors did not report the Ag:Pt ratio in their particles [82].

Regardless of the presence or absence of a sacrificial anode effect, the cytotoxicity of silver-containing nanoparticles has always been related to the release of silver ions [11,13,83,84]. In most studies, the silver-containing nanoparticles were surface-stabilized by ligands with low surface affinity, e.g., PVP. The low cytotoxicity of GSH-stabilized silver nanoparticles indicates that the surface ligand plays a decisive role in the cytotoxicity. The observed very low dissolution rate of GSH-coated silver nanoparticles is in line with earlier

results where PVP-coated silver nanoparticles (70 nm) did not show a release of silver ions in the presence of cysteine [55]. Cysteine obviously blocked the surface of the metal nanoparticles by firm adsorption, replacing the initial ligand PVP. This was also found by Liu et al. and Levard et al., who reviewed different approaches to control the release of silver ions from silver nanoparticles. They concluded that the release of silver ions is restricted by sulfidation or by thiol ligands on the silver nanoparticle surface [57,85–87]. It has been shown by various methods that the sulfur–silver bond is very strong [30,72,88,89] and apparently prevents the release of silver ions by oxidation. It should also be considered that the ligand density on the surface of an ultrasmall nanoparticle is very high (14 to 29 GSH units per nm²); i.e., the metal surface is probably well protected against oxidative attack from dissolved oxygen. This is obviously also the case for ultrasmall nanoparticles with their very high specific surface area. The oxidized state of the particles as shown by XPS for both silver and for platinum implies the presence of oxidized surface species, probably together with glutathione via the sulfur atom. However, it must be cautioned that the dissolution in water may be different from that in cell culture media where a complexation of silver ions by proteins or other biomolecules is well conceivable. Unfortunately, it is not possible to study the dissolution of ultrasmall silver nanoparticles in biological media like RPMI-FCS because particles and ions cannot be separated in the presence of high protein concentrations (nanoparticles and proteins are of the same dimension and cannot be separated by spin filtration) [24].

It is remarkable that the highest cytotoxicity against eukaryotic cells and bacteria was observed for the bimetallic nanoparticles, especially with an equimolar ratio of silver to platinum. They were much more cytotoxic than a physical mixture of the monometallic nanoparticles. This cannot be ascribed to the thiolated surface which is also present in monometallic silver nanoparticles. Although the exact mechanism of the cytotoxic action is not known, it is likely that the oxidized nature of the metals (especially of silver) influences the biological effects, possibly after cellular uptake.

5. Conclusions

All types of ultrasmall nanoparticles are easily taken up by eukaryotic cells (HeLa), regardless of the composition of their metal core. Bimetallic nanoparticles have a higher cytotoxicity and a stronger bactericidal effect than a physical mixture of silver and platinum nanoparticles and the monometallic nanoparticles, both against HeLa cells and bacteria (*E. coli*, Gram-negative, and *S. xylosus*, Gram-positive). This is not due to an enhanced dissolution, e.g., by an oxidative release of silver ions. The very dense surface coverage by the strongly attached ligand glutathione (bound by the strong Ag-S bond) is probably responsible for the very low release of silver ions. Nevertheless, the fact that the bimetallic nanoparticles are consistently more cytotoxic than the monometallic silver nanoparticles, although both do not release silver ions upon immersion in water, must be due their bimetallic nature. Obviously, the bimetallic AgPt nanoparticles exert an additional cytotoxic effect which occurs only in biological media and cannot be explained by the ion release in water. It is well conceivable that an enhanced dissolution mediated by biomolecules and increased by polarization of silver by platinum is responsible for this effect.

Supplementary Materials: The following supporting information can be downloaded at: <https://www.mdpi.com/article/10.3390/ma17153702/s1>: Figure S1: Differential centrifugal sedimentation (DCS) of bimetallic Ag₇₀Pt₃₀ and Ag₂₀Pt₈₀ nanoparticles; Figure S2: SAXS on bimetallic Ag₇₀Pt₃₀ and Ag₂₀Pt₈₀ nanoparticles; Figure S3: X-ray powder diffraction on bimetallic Ag₇₀Pt₃₀ and Ag₂₀Pt₈₀ nanoparticles; Figure S4: XPS measurements on bimetallic Ag₇₀Pt₃₀ and Ag₂₀Pt₈₀ nanoparticles; Figure S5: ¹H NMR spectra of Ag₇₀Pt₃₀ and Ag₂₀Pt₈₀ nanoparticles; Figure S6: ¹³C-DEPTQ NMR spectra of Ag₇₀Pt₃₀ and Ag₂₀Pt₈₀ nanoparticles; Figure S7: ¹H-¹H COSY NMR spectra of Ag₇₀Pt₃₀ and Ag₂₀Pt₈₀ nanoparticles; Figure S8: ¹H-¹³C HSQC NMR spectra of Ag₇₀Pt₃₀ and Ag₂₀Pt₈₀ nanoparticles; Figure S9: ¹H-¹³C-HMBC NMR spectra of Ag₇₀Pt₃₀ and Ag₂₀Pt₈₀ nanoparticles; Figure S10: IR spectra of GSH- und N₃-terminated gold, silver, platinum, and bimetallic silver-platinum nanoparticles.

Author Contributions: Conceptualization, M.E. and M.H.; methodology, N.W., N.B., K.L., M.H., T.S., F.N., C.W., C.B., P.B., O.P., C.L.P.O. and M.E.; investigation, N.W., N.B., K.L., M.H., T.S., F.N., C.W., C.B., P.B., O.P., C.L.P.O. and M.E.; writing—original draft preparation, N.W., N.B., K.L., M.H., T.S., F.N., C.W., C.B., P.B., O.P., C.L.P.O. and M.E.; writing—review and editing, N.W., N.B., K.L., M.H., T.S., F.N., C.W., C.B., P.B., O.P., C.L.P.O. and M.E.; supervision, M.H., C.L.P.O. and M.E.; project administration, M.H. and M.E.; funding acquisition, M.H., M.E. and C.L.P.O. All authors have read and agreed to the published version of the manuscript.

Funding: M.E. and M.H. are grateful to the Deutsche Forschungsgemeinschaft (DFG) for funding in the projects EP 22/62-1 and HE 7192/8-1. M.E. and C.L.P.O. are grateful to the German Academic Exchange Service (DAAD) and Fundação Coordenação de Aperfeiçoamento de Pessoal de Nível Superior (CAPES, Finance Code 001) for funding of a joint project in the framework of PROBRAL/PPP. This study was financed in part by the Coordenação de Aperfeiçoamento de Pessoal de Nível Superior—Brasil (CAPES), Finance Code 001. C.L.P.O. is supported by São Paulo Research Foundation (FAPESP) grant #2016/24531-3, Conselho Nacional de Desenvolvimento Científico e Tecnológico (CNPq) grant #303001/2019-4, and INCT-FCx (Instituto Nacional de Ciência e Tecnologia de Fluidos Complexos).

Institutional Review Board Statement: Not applicable.

Informed Consent Statement: Not applicable.

Data Availability Statement: The original contributions presented in the study are included in the article/Supplementary Material; further inquiries can be directed to the corresponding author.

Acknowledgments: We thank Beate Römer and Robin Meya for elemental analyses and the EMUSAXS technicians Igino Martins and Gabriel B. M. Teobaldo for support with the SAXS data acquisition. Sebastian Leiting (MPI für Kohlenforschung) is acknowledged for the XPS measurements.

Conflicts of Interest: The authors declare no conflicts of interest.

References

1. Bhatia, S.N.; Chen, X.; Dobrovolskaia, M.A.; Lammers, T. Cancer nanomedicine. *Nat. Rev. Cancer* **2022**, *22*, 550–556. [[CrossRef](#)] [[PubMed](#)]
2. Van der Meel, R.; Sulheim, E.; Shi, Y.; Kiessling, F.; Mulder, W.J.M.; Lammers, T. Smart cancer nanomedicine. *Nat. Nanotechnol.* **2019**, *14*, 1007–1017. [[CrossRef](#)]
3. Pelaz, B.; Alexiou, C.; Alvarez-Puebla, R.A.; Alves, F.; Andrews, A.M.; Ashraf, S.; Balogh, L.P.; Ballerini, L.; Bestetti, A.; Brendel, C.; et al. Diverse applications of nanomedicine. *ACS Nano* **2017**, *11*, 2313–2381. [[CrossRef](#)]
4. Agatea, L.; Crotti, S.; Ragazzi, E.; Bedin, C.; Urso, E.; Mammi, I.; Traldi, P.; Pucciarelli, S.; Nitti, D.; Agostini, M. Peptide patterns as discriminating biomarkers in plasma of patients with familial adenomatous polyposis. *Clin. Color. Cancer* **2016**, *15*, e75–e92. [[CrossRef](#)] [[PubMed](#)]
5. Tang, W.; Fan, W.; Lau, J.; Deng, L.; Shen, Z.; Chen, X. Emerging blood-brain-barrier-crossing nanotechnology for brain cancer theranostics. *Chem. Soc. Rev.* **2019**, *48*, 2967–3014. [[CrossRef](#)] [[PubMed](#)]
6. Gao, X.L.; Guo, L.H.; Li, J.Q.; Thu, H.E.; Hussain, Z. Nanomedicines guided nanoimaging probes and nanotherapeutics for early detection of lung cancer and abolishing pulmonary metastasis: Critical appraisal of newer developments and challenges to clinical transition. *J. Control. Release* **2018**, *292*, 29–57. [[CrossRef](#)]
7. Wolfbeis, O.S. An overview of nanoparticles commonly used in fluorescent bioimaging. *Chem. Soc. Rev.* **2015**, *44*, 4743–4768. [[CrossRef](#)]
8. Eleraky, N.E.; Allam, A.; Hassan, S.B.; Omar, M.M. Nanomedicine fight against antibacterial resistance: An overview of the recent pharmaceutical innovations. *Pharmaceutics* **2020**, *12*, 142. [[CrossRef](#)]
9. Slavin, Y.N.; Asnis, J.; Häfeli, U.O.; Bach, H. Metal nanoparticles: Understanding the mechanisms behind antibacterial activity. *J. Nanobiotechnol.* **2017**, *15*, 65. [[CrossRef](#)]
10. Rice, K.M.; Ginjupalli, G.K.; Manne, N.; Jones, C.B.; Blough, E.R. A review of the antimicrobial potential of precious metal derived nanoparticle constructs. *Nanotechnology* **2019**, *30*, 372001. [[CrossRef](#)]
11. Duran, N.; Duran, M.; de Jesus, M.B.; Seabra, A.B.; Favaro, W.J.; Nakazato, G. Silver nanoparticles: A new view on mechanistic aspects on antimicrobial activity. *Nanomedicine* **2016**, *12*, 789–799. [[CrossRef](#)] [[PubMed](#)]
12. Franci, G.; Falanga, A.; Galdiero, S.; Palomba, L.; Rai, M.; Morelli, G.; Galdiero, M. Silver nanoparticles as potential antibacterial agents. *Molecules* **2015**, *20*, 8856–8874. [[CrossRef](#)]
13. Chernousova, S.; Eppler, M. Silver as antibacterial agent: Ion, nanoparticle, metal. *Angew. Chem. Int. Ed.* **2013**, *52*, 1636–1653. [[CrossRef](#)]

14. Greulich, C.; Braun, D.; Peetsch, A.; Diendorf, J.; Siebers, B.; Epple, M.; Koller, M. The toxic effect of silver ions and silver nanoparticles towards bacteria and human cells occurs in the same concentration range. *RSC Adv.* **2012**, *2*, 6981–6987. [\[CrossRef\]](#)
15. Streich, C.; Stein, F.; Jakobi, J.; Ingendoh-Tsakmakidis, A.; Heine, N.; Rehbock, C.; Winkel, A.; Grade, S.; Kühnel, M.; Migunov, V.; et al. The origin of the intracellular silver in bacteria: A comprehensive study using targeting gold-silver alloy nanoparticles. *Adv. Healthc. Mater.* **2023**, *12*, 2302084. [\[CrossRef\]](#)
16. Guisbiers, G.; Mendoza-Cruz, R.; Bazan-Diaz, L.; Velazquez-Salazar, J.J.; Mendoza-Perez, R.; Robledo-Torres, J.A.; Rodriguez-Lopez, J.L.; Montejano-Carrizales, J.M.; Whetten, R.L.; Jose-Yacaman, M. Electrum, the gold–silver alloy, from the bulk scale to the nanoscale: Synthesis, properties, and segregation rules. *ACS Nano* **2016**, *10*, 188–198. [\[CrossRef\]](#)
17. Al-Zubeidi, A.; Stein, F.; Flatebo, C.; Rehbock, C.; Hosseini Jebeli, S.A.; Landes, C.F.; Barcikowski, S.; Link, S. Single-particle hyperspectral imaging reveals kinetics of silver ion leaching from alloy nanoparticles. *ACS Nano* **2021**, *15*, 8363–8375. [\[CrossRef\]](#)
18. Grasmik, V.; Rurainsky, C.; Loza, K.; Evers, M.V.; Prymak, O.; Heggen, M.; Tschulik, K.; Epple, M. Deciphering the surface composition and the internal structure of alloyed silver–gold nanoparticles. *Chem. Eur. J.* **2018**, *24*, 9051–9060. [\[CrossRef\]](#) [\[PubMed\]](#)
19. Ristig, S.; Chernousova, S.; Meyer-Zaika, W.; Epple, M. Synthesis, characterization and in-vitro effects of 7 nm alloyed silver-gold nanoparticles. *Beilstein J. Nanotechnol.* **2015**, *6*, 1212–1220. [\[CrossRef\]](#) [\[PubMed\]](#)
20. Sotiriou, G.A.; Etterlin, G.D.; Spyrogianni, A.; Krumeich, F.; Leroux, J.C.; Pratsinis, S.E. Plasmonic biocompatible silver-gold alloyed nanoparticles. *Chem. Commun.* **2014**, *50*, 13559–13562. [\[CrossRef\]](#)
21. Breisch, M.; Grasmik, V.; Loza, K.; Pappert, K.; Rostek, A.; Ziegler, N.; Ludwig, A.; Heggen, M.; Epple, M.; Tiller, J.C.; et al. Bimetallic silver platinum nanoparticles with combined osteo-promotive and antimicrobial activity. *Nanotechnology* **2019**, *30*, 305101. [\[CrossRef\]](#)
22. Grasmik, V.; Breisch, M.; Loza, K.; Heggen, M.; Köller, M.; Sengstock, C.; Epple, M. Synthesis and biological characterization of alloyed silver–platinum nanoparticles: From compact core–shell nanoparticles to hollow nanoalloys. *RSC Adv.* **2018**, *8*, 38582–38590. [\[CrossRef\]](#)
23. Ryu, H.S.; Bae, I.H.; Lee, K.G.; Hwang, H.S.; Lee, K.H.; Koh, J.T.; Cho, J.H. Antibacterial effect of silver-platinum coating for orthodontic appliances. *Angle Orthod.* **2012**, *82*, 151–157. [\[CrossRef\]](#)
24. Epple, M.; Rotello, V.M.; Dawson, K. The why and how of ultrasmall nanoparticles. *Acc. Chem. Res.* **2023**, *56*, 3369–3378. [\[CrossRef\]](#)
25. Klein, K.; Loza, K.; Heggen, M.; Epple, M. An efficient method for covalent surface functionalization of ultrasmall metallic nanoparticles by surface azidation, followed by copper-catalyzed azide-alkyne cycloaddition. *ChemNanoMat* **2021**, *7*, 1330–1339. [\[CrossRef\]](#)
26. Thust, A.; Barthel, J.; Tillmann, K. FEI Titan 80–300 TEM. *J. Large-Scale Res. Facil.* **2016**, *2*, A41. [\[CrossRef\]](#)
27. Hammersley, A.P. FIT2D: A multi-purpose data reduction, analysis and visualization program. *J. Appl. Crystallogr.* **2016**, *49*, 646–652. [\[CrossRef\]](#)
28. Oliveira, C.L.P.; Vorup-Jensen, T.; Andersen, C.B.F.; Andersen, G.R.; Pedersen, J.S. Discovering new features of protein complexes structures by small-angle X-ray scattering. In *Applications of Synchrotron Light to Scattering and Diffraction in Materials and Life Sciences*; Gomez, M., Nogales, A., Garcia-Gutierrez, M.C., Ezquerra, T.A., Eds.; Springer: Berlin/Heidelberg, Germany, 2009; pp. 231–244.
29. Garcia, P.R.A.F.; Prymak, O.; Grasmik, V.; Pappert, K.; Wlysses, W.; Otubo, L.; Epple, M.; Oliveira, C.L.P. An in situ SAXS investigation of the formation of silver nanoparticles and bimetallic silver–gold nanoparticles in controlled wet-chemical reduction synthesis. *Nanoscale Adv.* **2019**, *2*, 225–238. [\[CrossRef\]](#)
30. Wolff, N.; Loza, K.; Heggen, M.; Schaller, T.; Niemeyer, F.; Bayer, P.; Beuck, C.; Oliveira, C.L.P.; Prymak, O.; Weidenthaler, C.; et al. Ultrastructure and surface composition of glutathione-terminated ultrasmall silver, gold, platinum, and alloyed silver–platinum nanoparticles (2 nm). *Inorg. Chem.* **2023**, *62*, 17470–17485. [\[CrossRef\]](#)
31. Stejskal, E.O.; Tanner, J.E. Spin diffusion measurements: Spin echoes in the presence of a time-dependent field gradient. *J. Chem. Phys.* **1965**, *42*, 288–292. [\[CrossRef\]](#)
32. Altieri, A.S.; Hinton, D.P.; Byrd, R.A. Association of biomolecular systems via pulsed-field gradient NMR self-diffusion measurements. *J. Am. Chem. Soc.* **1995**, *117*, 7566–7567. [\[CrossRef\]](#)
33. Einstein, A. Über die von der molekularkinetischen Theorie der Wärme geforderte Bewegung von in ruhenden Flüssigkeiten suspendierten Teilchen. *Ann. Phys.* **1905**, *322*, 549–560. [\[CrossRef\]](#)
34. Fairley, N.; Fernandez, V.; Richard-Plouet, M.; Guillot-Deudon, C.; Walton, J.; Smith, E.; Flahaut, D.; Greiner, M.; Biesinger, M.; Tougaard, S.; et al. Systematic and collaborative approach to problem solving using X-ray photoelectron spectroscopy. *Appl. Surf. Sci. Adv.* **2021**, *5*, 100112. [\[CrossRef\]](#)
35. Van der Meer, S.B.; Loza, K.; Wey, K.; Heggen, M.; Beuck, C.; Bayer, P.; Epple, M. Click chemistry on the surface of ultrasmall gold nanoparticles (2 nm) for covalent ligand attachment followed by NMR spectroscopy. *Langmuir* **2019**, *35*, 7191–7204. [\[CrossRef\]](#)
36. Brust, M.; Fink, J.; Bethell, D.; Schiffrin, D.J.; Kiely, C. Synthesis and reactions of functionalised gold nanoparticles. *J. Chem. Soc. Chem. Commun.* **1995**, 1655–1656. [\[CrossRef\]](#)
37. Liz-Marzan, L.M. Gold nanoparticle research before and after the Brust–Schiffrin method. *Chem. Comm.* **2013**, *49*, 16–18. [\[CrossRef\]](#)

38. Ferreira, R.S.; Lira, A.L.; Torquato, R.J.S.; Schuck, P.; Sousa, A.A. Mechanistic insights into ultrasmall gold nanoparticle-protein interactions through measurement of binding kinetics. *J. Phys. Chem. C* **2019**, *123*, 28450–28459. [[CrossRef](#)]
39. Calborean, A.; Martin, F.; Marconi, D.; Turcu, R.; Kacso, I.E.; Buimaga-Iarinca, L.; Graur, F.; Turcu, I. Adsorption mechanisms of L-glutathione on Au and controlled nano-patterning through Dip Pen Nanolithography. *Mater. Sci. Eng. C* **2015**, *57*, 171–180. [[CrossRef](#)]
40. Fissan, H.; Ristig, S.; Kaminski, H.; Asbach, C.; Eppe, M. Comparison of different characterization methods for nanoparticle dispersions before and after aerosolization. *Anal. Methods* **2014**, *6*, 7324–7334. [[CrossRef](#)]
41. Wolff, N.; Beuck, C.; Schaller, T.; Eppe, M. Possibilities and limitations of solution-state NMR spectroscopy to analyze the ligand shell of ultrasmall metal nanoparticles. *Nanoscale Adv.* **2024**, *6*, 3285–3298. [[CrossRef](#)]
42. Rostovtsev, V.V.; Green, L.G.; Fokin, V.V.; Sharpless, K.B. A stepwise Huisgen cycloaddition process: Copper(I)-catalyzed regioselective “ligation” of azides and terminal alkynes. *Angew. Chem. Int. Ed.* **2002**, *41*, 2596–2599. [[CrossRef](#)]
43. Klein, K.; Hayduk, M.; Kollenda, S.; Schmiedtchen, M.; Voskuhl, J.; Eppe, M. Covalent attachment of aggregation-induced emission molecules to the surface of ultrasmall gold nanoparticles to enhance cell penetration. *Molecules* **2022**, *27*, 1788. [[CrossRef](#)]
44. Yu, R.; Liz-Marzan, L.M.; Garcia de Abajo, F.J. Universal analytical modeling of plasmonic nanoparticles. *Chem. Soc. Rev.* **2017**, *46*, 6710–6724. [[CrossRef](#)]
45. Mosmann, T. Rapid colorimetric assay for cellular growth and survival: Application to proliferation and cytotoxicity assays. *J. Immunol. Methods* **1983**, *65*, 55–63. [[CrossRef](#)]
46. Cui, Z.H.; He, H.L.; Wu, S.B.; Dong, C.L.; Lu, S.Y.; Shan, T.J.; Fang, L.X.; Liao, X.P.; Liu, Y.H.; Sun, J. Rapid screening of essential oils as substances which enhance antibiotic activity using a modified well diffusion method. *Antibiotics* **2021**, *10*, 463. [[CrossRef](#)]
47. Ding, W.; Zhou, Y.; Qu, Q.; Cui, W.; God’spower, B.O.; Liu, Y.; Chen, X.; Chen, M.; Yang, Y.; Li, Y. Azithromycin inhibits biofilm formation by *Staphylococcus xylosus* and affects histidine biosynthesis pathway. *Front. Pharmacol.* **2018**, *9*, 740. [[CrossRef](#)]
48. Tashiro, Y.; Eida, H.; Ishii, S.; Futamata, H.; Okabe, S. Generation of small colony variants in biofilms by *Escherichia coli* harboring a conjugative F plasmid. *Microbes Environ.* **2017**, *32*, 40–46. [[CrossRef](#)]
49. Sikder, M.; Lead, J.R.; Chandler, G.T.; Baalousha, M. A rapid approach for measuring silver nanoparticle concentration and dissolution in seawater by UV-Vis. *Sci. Total Environ.* **2018**, *618*, 597–607. [[CrossRef](#)]
50. Loza, K.; Eppe, M. Silver nanoparticles in complex media: An easy procedure to discriminate between metallic silver nanoparticles, reprecipitated silver chloride, and dissolved silver species. *RSC Adv.* **2018**, *8*, 24386–24391. [[CrossRef](#)]
51. Graf, C.; Nordmeyer, D.; Sengstock, C.; Ahlberg, S.; Diendorf, J.; Raabe, J.; Eppe, M.; Köller, M.; Lademann, J.; Vogt, A.; et al. Shape-dependent dissolution and cellular uptake of silver nanoparticles. *Langmuir* **2018**, *34*, 1506–1519. [[CrossRef](#)]
52. Merrifield, R.C.; Stephan, C.; Lead, J. Determining the concentration dependent transformations of Ag nanoparticles in complex media: Using SP-ICP-MS and Au@Ag core shell nanoparticles as tracers. *Environ. Sci. Technol.* **2017**, *51*, 3206–3213. [[CrossRef](#)] [[PubMed](#)]
53. Kaiser, J.P.; Roesslein, M.; Diener, L.; Wichser, A.; Nowack, B.; Wick, P. Cytotoxic effects of nanosilver are highly dependent on the chloride concentration and the presence of organic compounds in the cell culture media. *J. Nanobiotechnol.* **2017**, *15*, 5. [[CrossRef](#)] [[PubMed](#)]
54. Adamczyk, Z.; Ocwieja, M.; Mrowiec, H.; Walas, S.; Lupa, D. Oxidative dissolution of silver nanoparticles: A new theoretical approach. *J. Colloid Interface Sci.* **2016**, *469*, 355–364. [[CrossRef](#)]
55. Loza, K.; Diendorf, J.; Greulich, C.; Ruiz-Gonzales, L.; Gonzalez-Calbet, J.M.; Vallet-Regi, M.; Koeller, M.; Eppe, M. The dissolution and biological effect of silver nanoparticles in biological media. *J. Mater. Chem. B* **2014**, *2*, 1634–1643. [[CrossRef](#)] [[PubMed](#)]
56. Ho, C.M.; Wong, C.K.; Yau, S.K.W.; Lok, C.N.; Che, C.M. Oxidative dissolution of silver nanoparticles by dioxygen: A kinetic and mechanistic study. *Chem. Asian J.* **2011**, *6*, 2506–2511. [[CrossRef](#)]
57. Liu, L.; Hurt, R.H. Ion release kinetics and particle persistence in aqueous nano-silver colloids. *Environ. Sci. Technol.* **2010**, *44*, 2169–2175. [[CrossRef](#)] [[PubMed](#)]
58. Kittler, S.; Greulich, C.; Diendorf, J.; Köller, M.; Eppe, M. Toxicity of silver nanoparticles increases during storage because of slow dissolution under release of silver ions. *Chem. Mater.* **2010**, *22*, 4548–4554. [[CrossRef](#)]
59. Ho, C.M.; Yau, S.K.W.; Lok, C.N.; So, M.H.; Che, C.M. Oxidative dissolution of silver nanoparticles by biologically relevant oxidants: A kinetic and mechanistic study. *Chem. Asian J.* **2010**, *5*, 285–293. [[CrossRef](#)]
60. Nazarenus, M.; Zhang, Q.; Soliman, M.G.; del Pino, P.; Pelaz, B.; Carregal-Romero, S.; Rejman, J.; Rothen-Rutishauser, B.; Clift, M.J.D.; Zellner, R.; et al. In vitro interaction of colloidal nanoparticles with mammalian cells: What have we learned thus far? *Beilstein J. Nanotechnol.* **2014**, *5*, 1477–1490. [[CrossRef](#)]
61. Patel, S.; Kim, J.; Herrera, M.; Mukherjee, A.; Kabanov, A.V.; Sahay, G. Brief update on endocytosis of nanomedicines. *Adv. Drug Deliv. Rev.* **2019**, *144*, 90–111. [[CrossRef](#)] [[PubMed](#)]
62. Huo, S.; Jin, S.; Ma, X.; Xue, X.; Yang, K.; Kumar, A.; Wang, P.C.; Zhang, J.; Hu, Z.; Liang, X.J. Ultrasmall gold nanoparticles as carriers for nucleus-based gene therapy due to size-dependent nuclear entry. *ACS Nano* **2014**, *8*, 5852–5862. [[CrossRef](#)]
63. Yang, L.; Shang, L.; Nienhaus, G.U. Mechanistic aspects of fluorescent gold nanocluster internalization by live HeLa cells. *Nanoscale* **2013**, *5*, 1537–1543. [[CrossRef](#)] [[PubMed](#)]
64. Carrillo-Carrion, C.; Bocanegra, A.I.; Arnaiz, B.; Feliu, N.; Zhu, D.C.; Parak, W.J. Triple-labeling of polymer-coated quantum dots and adsorbed proteins for tracing their fate in cell cultures. *ACS Nano* **2019**, *13*, 4631–4639. [[CrossRef](#)]

65. Sokolova, V.; Ebel, J.F.; Kollenda, S.; Klein, K.; Kruse, B.; Veltkamp, C.; Lange, C.M.; Westendorf, A.M.; Eppele, M. Uptake of functional ultrasmall gold nanoparticles in 3D gut cell models. *Small* **2022**, *18*, 2201167. [[CrossRef](#)] [[PubMed](#)]
66. Hosseini, S.; Wetzel, O.; Kostka, K.; Heggen, M.; Loza, K.; Eppele, M. Pathways for oral and rectal delivery of gold nanoparticles (1.7 nm) and gold nanoclusters into the colon: Enteric-coated capsules and suppositories. *Molecules* **2021**, *26*, 5069. [[CrossRef](#)] [[PubMed](#)]
67. Schmid, G.; Kreyling, W.G.; Simon, U. Toxic effects and biodistribution of ultrasmall gold nanoparticles. *Arch. Toxicol.* **2017**, *91*, 3011–3037. [[CrossRef](#)]
68. Rostek, A.; Breisch, M.; Pappert, K.; Loza, K.; Heggen, M.; Köller, M.; Sengstock, C.; Eppele, M. Comparative biological effects of spherical noble metal nanoparticles (Rh, Pd, Ag, Pt, Au) with 4–8 nm diameter. *Beilstein J. Nanotechnol.* **2018**, *9*, 2763–2774. [[CrossRef](#)]
69. Helmlinger, J.; Sengstock, C.; Gross-Heitfeld, C.; Mayer, C.; Schildhauer, T.A.; Köller, M.; Eppele, M. Silver nanoparticles with different size and shape: Equal cytotoxicity, but different antibacterial effects. *RSC Adv.* **2016**, *6*, 18490–18501. [[CrossRef](#)]
70. Loza, K.; Sengstock, C.; Chernousova, S.; Koeller, M.; Eppele, M. The predominant species of ionic silver in biological media is colloidal dispersed nanoparticulate silver chloride. *RSC Adv.* **2014**, *4*, 35290–35297. [[CrossRef](#)]
71. Ahlberg, S.; Meinke, M.C.; Werner, L.; Eppele, M.; Diendorf, J.; Blume-Peytavi, U.; Lademann, J.; Vogt, A.; Rancan, F. Comparison of silver nanoparticles stored under air or argon with respect to the induction of intracellular free radicals and toxic effects toward keratinocytes. *Eur. J. Pharm. Biopharm.* **2014**, *88*, 651–657. [[CrossRef](#)]
72. Wetzel, O.; Hosseini, S.; Loza, K.; Heggen, M.; Prymak, O.; Bayer, P.; Beuck, C.; Schaller, T.; Niemeyer, F.; Weidenthaler, C.; et al. Metal–ligand interface and internal structure of ultrasmall silver nanoparticles (2 nm). *J. Phys. Chem. B* **2021**, *125*, 5645–5659. [[CrossRef](#)]
73. Breisch, M.; Loza, K.; Pappert, K.; Rostek, A.; Rurainsky, C.; Tschulik, K.; Heggen, M.; Eppele, M.; Tiller, J.C.; Schildhauer, T.A.; et al. Enhanced dissolution of silver nanoparticles in a physical mixture with platinum nanoparticles based on the sacrificial anode effect. *Nanotechnology* **2020**, *31*, 055703. [[CrossRef](#)] [[PubMed](#)]
74. Singh, C.; Mehata, A.K.; Priya, V.; Malik, A.K.; Setia, A.; Suseela, M.N.L.; Vikas; Gokul, P.; Samridhi; Singh, S.K.; et al. Bimetallic Au–Ag nanoparticles: Advanced nanotechnology for tackling antimicrobial resistance. *Molecules* **2022**, *27*, 7059. [[CrossRef](#)]
75. Cipriano, L.A.; Kristoffersen, H.H.; Munhos, R.L.; Pittkowski, R.; Arenz, M.; Rossmeisl, J. Tuning the chemical composition of binary alloy nanoparticles to prevent their dissolution. *Nanoscale* **2023**, *15*, 16697–16705. [[CrossRef](#)]
76. Chang, Y.; Cheng, Y.; Feng, Y.L.; Li, K.; Jian, H.; Zhang, H.Y. Upshift of the d band center toward the Fermi level for promoting silver ion release, bacteria inactivation, and wound healing of alloy silver nanoparticles. *ACS Appl. Mater. Interfaces* **2019**, *11*, 12224–12231. [[CrossRef](#)] [[PubMed](#)]
77. Abuayyash, A.; Ziegler, N.; Gessmann, J.; Sengstock, C.; Schildhauer, T.A.; Ludwig, A.; Köller, M. Antibacterial efficacy of sacrificial anode thin films combining silver with platinum group elements within a bacteria-containing human plasma clot. *Adv. Eng. Mater.* **2018**, *20*, 1700493. [[CrossRef](#)]
78. Koeller, M.; Bellova, P.; Javid, S.M.; Motemani, Y.; Khare, C.; Sengstock, C.; Tschulik, K.; Schildhauer, T.A.; Ludwig, A. Antibacterial activity of microstructured sacrificial anode thin films by combination of silver with platinum group elements (platinum, palladium, iridium). *Mater. Sci. Eng. C* **2017**, *74*, 536–541. [[CrossRef](#)]
79. El Arrassi, A.; Bellova, P.; Memar Javid, S.; Motemani, Y.; Khare, C.; Sengstock, C.; Köller, M.; Ludwig, A.; Tschulik, K. A unified interdisciplinary approach to design superior antibacterial coatings for fast silver release. *ChemElectroChem* **2017**, *4*, 1975–1983. [[CrossRef](#)]
80. Köller, M.; Sengstock, C.; Motemani, Y.; Khare, C.; Buenconsejo, P.J.S.; Geukes, J.; Schildhauer, T.A.; Ludwig, A. Antibacterial activity of microstructured Ag/Au sacrificial anode thin films. *Mater. Sci. Eng. C* **2015**, *46*, 276–280. [[CrossRef](#)]
81. Yang, L.; Chen, L.; Chen, Y.C.; Kang, L.; Yu, J.; Wang, Y.; Lu, C.; Mashimo, T.; Yoshiasa, A.; Lin, C.H. Homogeneously alloyed nanoparticles of immiscible Ag–Cu with ultrahigh antibacterial activity. *Colloids Surf. B Biointerfaces* **2019**, *180*, 466–472. [[CrossRef](#)]
82. Singh, A.V.; Patil, R.; Kasture, M.B.; Gade, W.N.; Prasad, B.L.V. Synthesis of Ag–Pt alloy nanoparticles in aqueous bovine serum albumin foam and their cytocompatibility against human gingival fibroblasts. *Colloids Surf. B Biointerfaces* **2009**, *69*, 239–245. [[CrossRef](#)]
83. Utembe, W.; Potgieter, K.; Stefaniak, A.B.; Gulumian, M. Dissolution and biodegradability: Important parameters needed for risk assessment of nanomaterials. *Part. Fibre Toxicol.* **2015**, *12*, 11. [[CrossRef](#)]
84. Ahlberg, S.; Antonopulos, A.; Diendorf, J.; Dringen, R.; Eppele, M.; Flöck, R.; Goedecke, W.; Graf, C.; Haberl, N.; Helmlinger, J.; et al. PVP-coated, negatively charged silver nanoparticles: A multi-center study of their physicochemical characteristics, cell culture and in vivo experiments. *Beilstein J. Nanotechnol.* **2014**, *5*, 1944–1965. [[CrossRef](#)]
85. Liu, J.; Sonshine, D.A.; Shervani, S.; Hurt, R.H. Controlled release of biologically active silver from nanosilver surfaces. *ACS Nano* **2010**, *4*, 6903–6913. [[CrossRef](#)]
86. Liu, J.Y.; Wang, Z.Y.; Liu, F.D.; Kane, A.B.; Hurt, R.H. Chemical transformations of nanosilver in biological environments. *ACS Nano* **2012**, *6*, 9887–9899. [[CrossRef](#)]
87. Levard, C.; Reinsch, B.C.; Michel, F.M.; Oumahi, C.; Lowry, G.V.; Brown, G.E. Sulfidation processes of PVP-coated silver nanoparticles in aqueous solution: Impact on dissolution rate. *Environ. Sci. Technol.* **2011**, *45*, 5260–5266. [[CrossRef](#)]

88. Pakiari, A.H.; Jamshidi, Z. Nature and strength of M-S bonds (M = Au, Ag, and Cu) in binary alloy gold clusters. *J. Phys. Chem. A* **2010**, *114*, 9212–9221. [[CrossRef](#)]
89. Marchioni, M.; Battocchio, C.; Joly, Y.; Gateau, C.; Nappini, S.; Pis, I.; Delangle, P.; Michaud-Soret, I.; Deniaud, A.; Veronesi, G. Thiolate-capped silver nanoparticles: Discerning direct grafting from sulfidation at the metal-ligand interface by interrogating the sulfur atom. *J. Phys. Chem. C* **2020**, *124*, 13467–13478. [[CrossRef](#)]

Disclaimer/Publisher's Note: The statements, opinions and data contained in all publications are solely those of the individual author(s) and contributor(s) and not of MDPI and/or the editor(s). MDPI and/or the editor(s) disclaim responsibility for any injury to people or property resulting from any ideas, methods, instructions or products referred to in the content.